

GAS-PHASE AND SOLUTION-PHASE PEPTIDE CONFORMATIONS
STUDIED BY ION MOBILITY - MASS SPECTROMETRY
AND MOLECULAR DYNAMICS SIMULATIONS

A Dissertation

by

LIUXI CHEN

Submitted to the Office of Graduate Studies of
Texas A&M University
in partial fulfillment of the requirements for the degree of

DOCTOR OF PHILOSOPHY

August 2012

Major Subject: Chemistry

Gas-phase and Solution-phase Peptide Conformations Studied by Ion Mobility-Mass
Spectrometry and Molecular Dynamics Simulations

Copyright 2012 Liuxi Chen

GAS-PHASE AND SOLUTION-PHASE PEPTIDE CONFORMATIONS
STUDIED BY ION MOBILITY - MASS SPECTROMETRY
AND MOLECULAR DYNAMICS SIMULATIONS

A Dissertation

by

LIUXI CHEN

Submitted to the Office of Graduate Studies of
Texas A&M University
in partial fulfillment of the requirements for the degree of

DOCTOR OF PHILOSOPHY

Approved by:

| | |
|---------------------|-----------------------|
| Chair of Committee, | David H. Russell |
| Committee Members, | Emile A. Schweikert |
| | Christian Hilty |
| | Jean-Philippe Pellois |
| Head of Department, | David H. Russell |

August 2012

Major Subject: Chemistry

ABSTRACT

Gas-phase and Solution-phase Peptide Conformations Studied by Ion Mobility-Mass Spectrometry and Molecular Dynamics Simulations. (August 2012)

Liuxi Chen, B.A., University of Science and Technology of China

Chair of Advisory Committee: Dr. David H. Russell

Ion mobility spectrometry (IMS) separates ions on the basis of ion-neutral collision cross-sections (Ω), which are determined by the geometry or conformation of the ions. The size-based IM separation can be extended to distinguish conformers that have different shapes in cases where shape differences influence the accessible surface area of the molecule. In recent years, IM has rapidly evolved as a structural characterization technique, which has applied on various structural biology problems. In this work, IMS is combined with molecular dynamics simulation (MDS), specially the integrated tempering sampling molecular dynamics simulation (ITS-MDS) to explore the gas-phase conformation space of two molecular systems (i) protonated tryptophan zipper 1 (trpzip1) ions and its six derivatives (ii) alkali metal ion (Na, K and Cs) adducts of gramicidin A (GA). The structural distributions obtained from ITS-MDS are compared well with results obtained from matrix-assisted laser desorption ionization-ion mobility-mass spectrometry (MALDI-IM-MS) for trpzip1 series and electrospray ionization-ion mobility-mass spectrometry (ESI-IM-MS) for alkali metal ion adducts of GA. Furthermore, the solvent dependence on conformational preferences of the GA

dimer is investigated using a combination of mass spectrometry techniques, *viz.* ESI-IM-MS and hydrogen/deuterium exchange (HDX)-MS, and MDS. The IM experiments reveal three distinct gramicidin A species, detected as the sodium ion adduct ions, $[2GA + 2Na]^{2+}$, and the equilibrium abundances of the dimer ions varies with solvent polarity. The solution phase conformations are assigned as the parallel and anti-parallel β -helix dimer, and the anti-parallel dimer is the preferred conformation in non-polar organic solvent. The calculated CCS profiles by ITS-MDS agree very well with the experimentally measured CCS profiles, which underscore the utility of the method for determining candidate structures as well as the relative abundances of the candidate structures. The benefit of combining ion mobility measurements with solution-phase H/D exchange is allowing identifications and detail analysis of the solution-phase subgroup conformations, which cannot be uncovered by one method alone.

This work is dedicated to my loving grandparents:

YongYi Zhang

JianSan Sun

JuYuan Gao

and

GuangZhong Chen (1928-2001)

ACKNOWLEDGEMENTS

I consider myself to be fortunate to come to the US for my graduate career, even more fortunate to be one of Dr David Russell's students. I have benefited so much from his guidance, wisdom, and most important of all enthusiasm for science. There are no words to express my deepest appreciation to him. In addition, I am also so grateful to learn from one of greatest theoretical chemists, Dr Yi Qin Gao. The state-of-art method I adapted from him changed the path of my graduate research.

I am also so thankful to work with many great and talented scientists and graduate students over the years. Special thanks to Dr. Kent Gillig, Dr William Russell, Dr Jody May, Dr Wenjian Sun, and Dr Lei Tao for their support and guidance on theory and application of ion mobility and mass spectrometry; to Dr Lisa Perez, Dr Qiang Shao, Dr Lijiang Yang for their knowledge on molecular dynamics simulations; to Dr Zhaoxiang Wu, Dr Brad Willisams, Dr Stephanie Cologna, Shu-hua Chen, Joshua Silveira, and Greg Matthijetz for helpful discussions and their support. I thank Dr Emile Schweikert, Dr Gyula Vigh, Dr Christian Hilty, and Dr Jean-Philippe Pellois for agreeing to serve on my defense committee.

I would like to thank my family for their loving support throughout my life and many years of education. I am so blessed to have wonderful parents, my mom Yihong Sun and my dad Jun Chen, who are always believing in me and encouraging me to be brave to pursue my dreams. I am everything I am because of them. My husband, Jiayi Jin, has been my closet friend, my greatest supporter ever since we met freshman year in

college. He is my strength when I am weak, my voice when I couldn't speak and my eyes when I could not see. He sees the best there is in me.

This work was supported by the National Science Foundation, the Robert A. Welch Foundation, and the U. S. Department of Energy, Division of Chemical Sciences.

NOMENCLATURE

| | |
|-------|---|
| IMS | Ion Mobility Spectrometry |
| MS | Mass Spectrometry |
| IM-MS | Ion Mobility-Mass Spectrometry |
| CCS | Collision Cross-Section |
| MDS | Molecular Dynamics Simulations |
| ITS | Integrated Tempering Sampling |
| REMD | Replica Exchange Molecular Dynamics |
| MALDI | Matrix-Assisted Laser Desorption Ionization |
| ESI | Electrospray Ionization |
| m/z | Mass-to-charge Ratio |
| ATD | Arrival Time Distribution |

TABLE OF CONTENTS

| | Page |
|--|------|
| ABSTRACT | iii |
| DEDICATION | v |
| ACKNOWLEDGEMENTS | vi |
| NOMENCLATURE | viii |
| TABLE OF CONTENTS | ix |
| LIST OF FIGURES | xi |
| LIST OF TABLES | xiii |
| CHAPTER | |
| I INTRODUCTION | 1 |
| II METHODS | 6 |
| Ion Mobility – Mass Spectrometry | 6 |
| Molecular Dynamics Simulations | 10 |
| Hydrogen/Deuterium Exchange | 14 |
| III GAS-PHASE CONFORMATIONS OF MODEL β -HAIRPIN PEPTIDE TRYPTOPHAN ZIPPER 1 | 16 |
| Introduction | 16 |
| Experimental Methods | 17 |
| Results and Discussion | 19 |
| Conclusions | 34 |
| IV THE EFFECT OF ALKALI METAL ION BINDING ON CONFORMATIONS OF GRAMICIDIN A | 37 |
| Introduction | 37 |
| Experimental Methods | 39 |
| Results and Discussion | 42 |

| CHAPTER | Page |
|--|------|
| Conclusions | 58 |
| V SOLUTION-PHASE CONFORMATIONS AND CONFORMATIONAL TRANSITION KINETICS OF GRAMICIDIN A..... | 60 |
| Introduction | 60 |
| Experimental Methods | 63 |
| Results and Discussion | 65 |
| Conclusions | 84 |
| VI SUMMARY | 87 |
| REFERENCES | 88 |
| VITA | 101 |

LIST OF FIGURES

| FIGURE | | Page |
|--------|---|------|
| 1 | Schematic of positive/negative mode MALDI ion mobility time-of-flight mass spectrometer. | 8 |
| 2 | Method flow chart of utilizing ITS-MDS to interpret IMS data | 13 |
| 3 | (A) The ITS-MDS free energy contour maps for each of the trpzip1 and its derivatives $[M + H]^+$ ions plotted as a function of backbone C α -rmsd and collision cross-section (CCS).(B) A 2-dimensional cross section or free energy profile representation of part (A). | 22 |
| 4 | Structural representation for most abundant clusters for H^+N (A), H^+N -acK ⁸ K ¹² (B), H^+K^8 (C), H^+K^8 -acNK ¹² (D), H^+K^{12} (E), and H^+K^{12} -acNK ⁸ (F). | 25 |
| 5 | The native-like γ -turn structures found in the simulation: cluster1 of H^+K^8 -acNK ¹² and cluster1 of H^+N | 26 |
| 6 | The structures of the most populated clusters for H^+N (A), H^+N -acK ⁸ K ¹² (B), H^+K^8 (C), H^+K^8 -acNK ¹² (D), H^+K^{12} (E), and H^+K^{12} -acNK ⁸ (F) and an enlarged view of the structures show the intramolecular interactions that stabilize each structural form for each molecule. | 28 |
| 7 | Plots of collision cross-section (CCS) profiles for three acetylated derivatives of trpzip1, H^+N -acK ⁸ K ¹² (A), H^+K^8 -acNK ¹² (B), and H^+K^{12} -acNK ⁸ (C). | 31 |
| 8 | Experimental (solid line) and calculated best-fits (dotted line) for the CCS profiles of $[Trpzip1 + H]^+$ | 33 |
| 9 | ITS-MDS derived conformations for neutral gramicidin A <i>in vacuo</i> . The population of each conformer is shown in the figure. | 43 |
| 10 | (A) The free energy landscape is plotted as a function of the potential energy and C α -RMSD for gramicidin A <i>in vacuo</i> . (B) Two-dimensional free energy profile representation of part (A). | 46 |
| 11 | ITS-MDS derived conformations, calculated CCSs, and cluster relative | |

| | | |
|----|---|----|
| | abundances for $[\text{GA} + \text{Na}]^+$, $[\text{GA} + \text{K}]^+$, and $[\text{GA} + \text{Cs}]^+$ | 49 |
| 14 | Backbone over-layed conformers of four clusters of $[\text{GA} + \text{Na}]^+$ ions with the corresponding neutral GA conformers. | 50 |
| 13 | Turn and β -sheet-forming tendencies of neutral GA and $[\text{GA} + \text{met}]^+$ (met = Na, K, Cs) as a function of GA amino acid sequence. | 52 |
| 14 | (A) Calculated collision cross-section profiles by ITS-MDS for the most populated clusters for $[\text{GA} + \text{met}]^+$. (B) Arrival time distributions of alkali metal (Na, K, Cs) adducts of gramicidin A. (C) Arrival time distributions of alkali metal (Na, K, Cs) adducts of des-formyl-gramicidin A. | 57 |
| 15 | (A) Zoom-in mass spectra of GA incubated in n-propanol as a function of time showing the m/z 1905 region of $[\text{GA} + \text{Na}]^+ / [2\text{GA} + 2\text{Na}]^{2+}$. (B) Ion mobility arrival time distributions of mass envelope of m/z 1905. | 66 |
| 16 | The kinetic profiles of the monomerization of GA at a concentration of 5 μM for a series of ethanol, propanol and isobutanol, expressed as the intensity ratio of monomers as a function of incubation time. | 67 |
| 17 | The kinetic profiles of three dimer conformers (D1, D2, D3) in ethanol (A), n-propanol (B), and isobutanol (C). | 69 |
| 18 | H/D back-exchange mass spectra of GA in n-propanol as function of time. The mass spectra contain two distinct mass envelopes of GA labeled as Mass Envelope A (ME_A) and Mass Envelopes B (ME_B). | 71 |
| 19 | Time-dependent change in deuterium content of GA monomer log scale.. | 74 |
| 20 | CID product ion spectrum of the $[\text{GA} + \text{Na} + 8]^+$ ion. | 76 |
| 21 | Collision cross section profiles of Mass Envelope A (ME_A) and Mass Envelope B (ME_B) of GA undergoing H/D back-exchange in n-propanol. only the GA dimer profiles are shown. | 81 |
| 22 | The comparison of calculated collision cross-sections of GA dimer candidate structures generated from PDB structures 1MIC (A), 1ALZ (B), and 1JNO (C) with experimental obtained CCS profiles. | 83 |

LIST OF TABLES

| TABLE | | Page |
|-------|---|------|
| 1 | The notation used to identify the derivatives of trpzip1, mass-to-charge ratios of the $[M + H]^+$ ions, experimental collision cross-sections (CCS) obtained by MALDI and ESI, calculated CCS values for the ions, and the percent γ -turn structure of the ion population. The notation H^+K^8 -acNK ¹² indicates protonation on the side chain of K ⁸ and both of the N-terminus and K ¹² are acetylated. | 20 |
| 2 | Relative abundances of three conformers (D1, D2, and D3) of GA dimer in ethanol, propanol and isobutanol at equilibrium. | 78 |

CHAPTER I

INTRODUCTION

While understanding protein structure and the processes that dictate protein folding/unfolding present enormous challenges to both experimentalists and theoreticians, studies that integrate computational and experimental approaches are providing new molecular level understanding of such processes.¹ In addition, new molecular level understanding of these processes have been realized from studies of *de novo* designed peptides,^{2,3} and protein fragments,⁴ which are aimed at examining the role(s) of “autonomous folding subunits”³, identifying “genuine folding intermediates” from structures of denatured states, and studies “intrinsically disordered peptides/proteins”.⁵⁻⁷ Protein structure(s)/biological function(s) relationships have important implications for studies of post-translational modification and the kinetics and thermodynamics of protein folding, aggregation, and self-assembly,⁸⁻¹⁰ however, all of these processes are also strongly influenced by both solvent and protein intramolecular interactions, *i.e.*, salt-bridges and proton bridges, hydrophobic interactions, and non-bonding-pi interactions.¹¹⁻¹³

The intra- and inter-molecular forces that dictate higher order structure of biomolecules remain as one of the major challenges of structural biology. Although there are numerous spectroscopic techniques, *i.e.*, circular dichroism (CD) and Raman, for investigating of complex molecules, these techniques report on conformer

This thesis follows the style of *Journal of the American Chemical Society*.

preferences averaged over the entire molecule and over the entire ensemble of conformers, thus short sequences or low abundances of local structure are oftentimes difficult to detect. Long-range interactions between distant regions of the protein affects the overall dimensions of the molecule, and these interactions can be probed by using dynamic light scattering, small angle X-ray scattering, fluorescence correlation spectroscopy and IM-MS. In addition, specialized NMR techniques such as residual dipolar coupling (RDC) are powerful biophysical tools that can be used to probe both local and long-range conformational behavior at atomic resolution and on very broad timescales.¹⁴ In addition, such techniques are often not able to reveal any information about one particular species of interest present in the complex mixture, because the signal is normally characteristic of the average of all components rather than one single component of interest, or data may be dominated by high abundance components.

Since the development of soft ionization techniques, electrospray (ESI)¹⁵ and matrix-assisted laser desorption/ionization (MALDI),^{16,17} introducing biomolecules into the gas phase as intact molecules, mass spectrometry (MS) has evolved into one of the most powerful bioanalytical tools. In addition, ESI allows introducing native oligomers/complexes into the gas-phase while native organization or geometrical preferences have been preserved.¹⁸⁻²⁰ MS analysis has some notable advantages, including sensitivity, speed, and the ability to analyze complex mixtures. Ion mobility spectrometry (IMS) separates ions on the basis of ion-neutral collision cross-sections (CCS, Ω), which are determined by the geometry or conformation of the ions. IMS-MS provides a unique way of simultaneous and direct analysis of the full profile of diverse

conformer populations in the mixture; enable more readily monitoring changes in the mixture. IMS data provide unique information about the overall shape and size of the molecular ions and combined with theoretical studies such electronic structure calculations and molecular dynamics (MD) simulations, more detail information about the three dimensional structures of molecules can be obtained.²¹⁻²⁶

In general, the difference between solution-phase conformations with gas-phase conformations, especially for small molecules or highly charged ions, can be substantial. Electrostatic interactions, which play an important role in defining three dimension structures of proteins, are stronger in the gas phase than in solution phase because they are not attenuated by the solvent. For example, water has a dielectric constant of 78 and it is able to effectively solvate the charge group. For the gas-phase protonated ions, the charge site interacts with other electronegative groups, mainly backbone carbonyl groups. In other words, in solution, the charge groups extend out and are solvated by the solvent, whereas in the gas phase, they fold back and expected to be solvated by the backbone.

Under experimental conditions favoring annealing into gas-phase conformations, gas-phase MD simulations should provide sufficient matching structures to the IM measurement data,²¹ which is the case for most MALDI generated ions. However, there are evidences that indicate that for a range of proteins, ESI-generated ions often retain significant aspects of their solution-phase structures, that is, in the absence of sufficient collisions, the structures of ESI-generated ions do not transit into its equilibrated gas-phase structures.^{22,27} Since proteins originate from solution, these ESI-generated ions are

likely to resemble solution-phase structures more closely than gas-phase structures. In those cases, solution-phase MD simulations of the molecules of interest have to be considered.

To obtain the three dimensional structures of molecules by IMS experiment, theoretical calculation predictions have to be applied. Typically, candidate structure selection is based on the ‘lowest energy structure’ from the many candidate conformations generated through multiple tiers of simulated annealing,^{25,26,28-30} however, the lowest energy structure obtained from simulated annealing may not accurately represent the total ion population, which is composed of an ensemble of conformations that may be limited to a particular set of experimental IMS conditions.^{27,31} We previously described a novel clustering algorithm that segregated the structural elements for candidate conformations generated by simulated annealing.³² The clustering method assigns candidate structures based on the similarities of backbone structure with an estimate of the uncertainty of the cluster membership and the degree of purity of the cluster. The advantage of this approach is that it provides a means of efficiently evaluating the entire candidate structure population generated by MDS. The limitation of this approach is that it does not provide information regarding the equilibrium ion conformational distribution (potential energy landscape)³³, which is essential for high confidence level structural assignments.

Various simulation methods have been applied to generate low-energy minima structures, to correlate the experimental determined CCS.^{30,32,34} In recent years, most commonly used method is molecular dynamics simulations (MDS), particularly

enhanced sampling MDS which have been developed to improve sampling efficiency and obtain thermodynamics properties. For example, replica exchange molecular dynamics (REMD) simulations have been successfully utilized to provide a detailed exploration of conformation space for polypeptide systems.^{19,35,36} Similar to REMD, integrated tempering sampling molecular dynamics simulations (ITS-MDS) developed by Gao,³⁷⁻⁴⁰ have proven to be an effective method to generate candidate structures as well as the free energy of the conformers to aid in interpreting experimental IMS data.^{21,22,31}

In the following chapters, three molecular systems studies by utilizing ion mobility-mass spectrometry and molecular dynamics will be presented. Chapters 3 and 4 demonstrated integrated tempering sampling-molecular dynamics simulations (ITS-MDS) combined with IMS is successfully used to characterize the gas-phase conformational space of two molecular systems: (i) a model β -hairpin peptide trpzip1 and three derivatives (acetylated lysine) of the peptide; (ii) alkali metal ion (Na, K and Cs) adducts of gramicidin A (GA). Chapter 5 presents a comprehensive study of combining ESI-IM-MS with MDS and H/D exchange to characterize the monomerization and dimeric conformational transition of GA to gain new insights of solution-phase GA self-assembled behavior.

CHAPTER II

METHODS

Ion Mobility – Mass Spectrometry

Ion mobility spectrometry (IMS) is an electrophoretic gas-phase separation technique, which has been applied to a wide range of analytical applications. In a conventional drift tube ion mobility experiment, ions drift through a region filled up with an inert gas, typically helium, under the influence of a weak electric field, in which ions are subjected to collisional heating as they traverse the IMS drift region. When the applied electric field is low, the steady flow of ions along the electric field is much lower than the random motion leading to diffusion. The drift velocity v_D at low field limits is proportional to the applied electric field E .^{41,42} The mobility K is the proportionality constant:

$$v_D = KE \quad (1)$$

The ions are separated on the basis of ion-neutral collision cross-section (CCS) or apparent surface area. CCS was calculated using the empirical drift time (t_d) based on the hard sphere approximation:

$$\Omega_{avg} = \frac{(18\pi)^{\frac{1}{2}}}{16} \frac{ze}{(k_b T)^{\frac{1}{2}}} \left(\frac{1}{m_i} + \frac{1}{m_b} \right)^{\frac{1}{2}} \frac{t_d E}{L} \frac{760}{P} \frac{T}{273.2} \frac{1}{N_0} \quad (2)$$

where z is the charge of the ion, e is elementary charge, k_b is Boltzmann's constant, m_i is the mass of the ion, m_b is the mass of buffer gas, E is the IM electric field strength, N_0 is

the number density of the drift gas at STP, L is the drift tube length, P is the buffer gas pressure and T is the system temperature.

The coupling of ion mobility to mass spectrometry (IM-MS) provides two-dimensional strategy for ultra-fast (us-ms time scale) post-ionization separation. Molecular classes tend to have slightly different correlation between collision cross-section and mass-to-charge, so that on the two dimension plot of size (collision cross-section) vs mass-to-charge, different molecular classes exhibit different “trendlines”. Our group and others successfully utilized IM-MS to screen chemically modified DNA molecules,⁴³ to distinguish between phosphorylated and nonphosphorylated peptides,^{44,45} to separate mixtures containing lipids, peptides and nucleotides,⁴⁶ to characterize synthetic polymer⁴⁷ as well as molecular structure analysis of crude petroleum extracts.⁴⁸

Another important feature of IM-MS is the m/z analysis of separated ion. It is important to show that the ‘analyte ions’ have not changed in m/z from that initially injected for IMS analysis. Also, fragmentation of IMS selected ions can provide additional structural information. By using collision-induced dissociation (CID)-capable IM-MS interface, Becker and coworkers have successfully fragmented and sequenced a number of peptide ions including peptides obtained by a tryptic digest.⁴⁹ Furthermore, surface-induced dissociation (SID) has also been successfully coupled to IM-MS in our group.⁵⁰⁻⁵² The IM-CID-MS and IM-SID-MS methods allow for the simultaneous determination of peptide mass, peptide-ion sequence, and collision-cross section providing information critical to the identification of unknown components in complex proteomic samples.

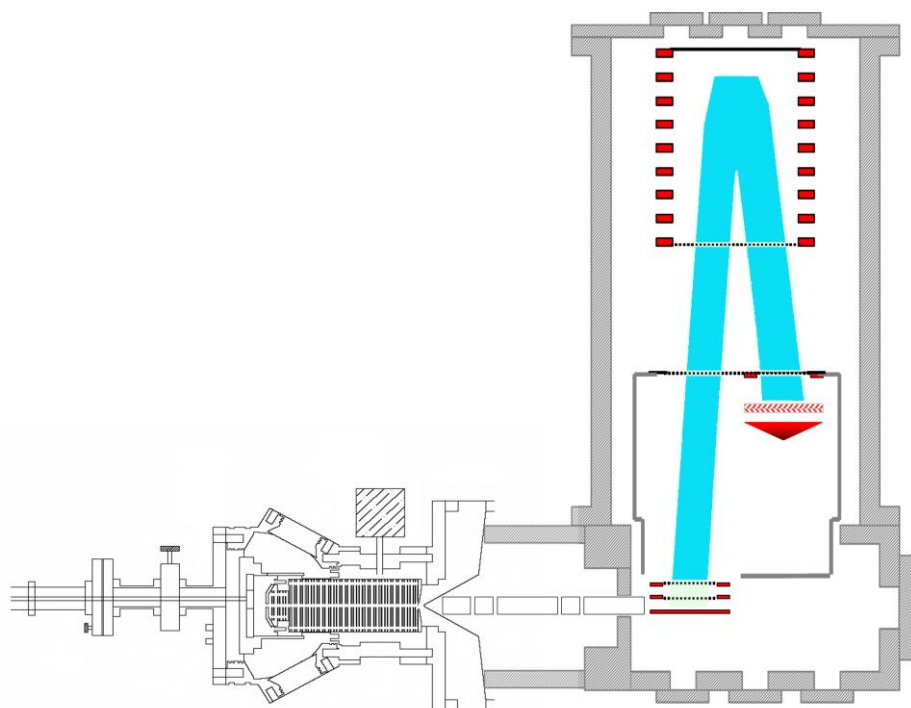


FIGURE 1. Schematic of positive/negative mode MALDI ion mobility time-of-flight mass spectrometer.

There are two types of IM-MS instruments used in the studies in the following chapters. First, the MALDI-IM-MS data were acquired using a home-built positive/negative MALDI-IM-time-of-flight (TOF) MS, which consists of a periodic focusing drift cell coupled to a high resolution reflectron time-of-flight as described previously.⁵³ A diagram of the instrument is shown in Figure 1. MALDI was performed using Nd:YAG (355nm) laser (CrystaLaser, Reno, NV) operated at a pulse rate of 300 Hz. The drift tube is 15 cm and maintained at a pressure of 1.5 torr He at room temperature. Mobility cell field strength is ranging from 16 to 36 V/cm·torr. The instrument polarity can be easily switched with minimal downtime. The mass spectrometer was externally calibrated using two-point calibration of the radical cations (+1) of C60 (Mr=720) and C70 (Mr=840) (Sigma). The 2D IM-MS data were acquired and process by custom software (Ionwerks, Inc).²⁵ Second, the ESI-IM-MS data were acquired on a Waters Synapt™ HDMS G2 mass spectrometer (Waters UK Ltd., Manchester, UK) equipped with a travelling-wave ion mobility cell maintained at 3 mbar of nitrogen. Ions were formed by nano-ESI using a source temperature of ~100 °C and capillary voltage 1.6-2.2 kV. A range of cone and the extraction voltages 5-100 V and 1-4 V, respectively, were used in the experiments (see below). For the IM experiments, the traveling wave ion mobility cell was operated at wave velocity of 550 m/s and wave amplitude of 38 V. Collision cross section (CCS) calibration was performed using methods described previously by Ruotolo et al.^{18,54} Calibration standards included tryptic digest peptides from cytochrome *c* and myoglobin. Literature values of CCS of calibrant peptides were taken from CCS database generated by Clemmer and coworkers.^{55,56}

In last two decades, ion mobility spectrometry (IMS) has rapidly evolved as a structural characterization technique,⁵⁷⁻⁵⁹ especially for systems that present a diverse population of conformers. For example, IMS provides a direct measure of the conformer preferences of solvent-free polypeptides,^{22,26,27,60} DNA complexes,⁶¹ large protein complexes,^{18,62} as well as oligomerization of protein fragments.^{19,35} Although determination of CCS via IMS measurement is relatively straightforward, it is more difficult to obtain structural information of the targeted molecular system from IM measurements. For large proteins or protein complexes, PDB structures of the same system from RCSB protein data bank are normally used to calculate theoretical CCS values and compare with the measured CCS values. Such approach relies on the assumption that proteins or protein complexes retain their three dimensional structures while being transferred from solution phase to gas phase. However, this is not the case, especially for small proteins or peptide ions, while gas-phase conformations are normally quite different from condensed-phase conformations. In latter case, interpretation of IMS data relies critically on conformation search strategies. Detailed simulation methods used are described in the following method section.

Molecular Dynamics Simulations

The integrated tempering sampling (ITS) method has been used in molecular dynamics simulations for polypeptides to enhance sampling in configuration space. The ITS method has been described previously^{38,39} and it has been previously applied to interpretation of IMS data.³¹ Briefly, the generalized distribution function, as a function of potential energy, $p(U)$, is written as an integration over β :

$$p(U) = \int_{\beta} f(\beta') e^{-\beta' U} d\beta' \quad (3)$$

where $\beta = \frac{1}{k_B T}$ (k_B is the Boltzmann constant and T is the temperature) and $f(\beta')$ is a normalizing function. MD simulation on modified potential U' (as a function of the original potential U) at the desired temperature corresponding to β , yields the distribution function:

$$e^{-\beta U'} = p(U) = \int_{\beta'} f(\beta') e^{-\beta' U} d\beta' \quad (4)$$

and the effective potential energy, U' , is:

$$U' = -\frac{1}{\beta} \int_{\beta'} f(\beta') e^{-\beta' U} d\beta' \quad (5)$$

The function $f(\beta')$ is estimated in ITS by a robust procedure in order to achieve an even sampling in the desired energy range.³⁹ The biased force in the MD simulation is then obtained as the derivative function of U' in Eq. 5. Thermodynamic properties of the system are finally calculated by reweighting corresponding terms with a weighting factor of $e^{\beta_0 (U' - U)}$.

AMBER force field parameters for modified amino acid residues which are not defined in the force field are derived using the R.E.D III program. The partial charge distribution on all atoms of the modified residues was derived by using the RESP method based on two structures (extended and α -helix) optimized at the quantum mechanics level of HF/6-31G+(d).^{63,64} The charge fitting was derived with the R.E.D III program.⁶⁵ MD simulations were performed using the AMBER 9.0 package. The AMBER FF96 or FF99SB all-atom force field was used for all standard amino acid

residues. MD simulations were performed *in-vacuo* at 300K which was maintained by using the weak-coupling algorithm with a coupling constant of 5.0 ps^{-1} . No non-bonded cutoff was used in simulations. For each case, six independent MD simulation trajectories with a length of 300 ns were obtained each starting from a different randomly generated initial structure.⁶⁶

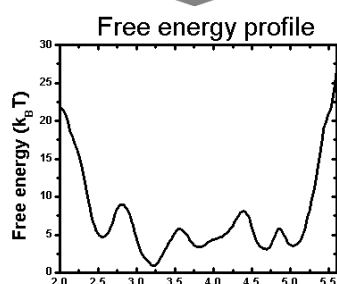
Clustering was based on the $C\alpha$ -rmsd and the cluster radius was selected as 3\AA using AMBER MMTSB tool set.⁶⁷ Thermodynamic properties of the system obtained from the ITS-MDS enable us to calculate the relative population of each cluster family, the CCS profile of which is further determined based on the centroid and standard deviation of CCS values and the relative population of each cluster.

The method flow chart of using the ITS-MDS to interpret IMS data is shown in Figure 2. First, ITS-MDS is performed on the desired sequence of the peptide in order to get free energy profile of the peptide. Based on the weighting factor and collision cross section of each structure, theoretical CCS profiles can be plotted. At the mean time, clustering can be done to find clusters with low free energy (high abundance). Second, the experimental profile is compared with the calculated profile, and conformer assignment of the experimental profile can be obtained. Last, free energy contour plot as a function of $C\alpha$ -rmsd and CCS can be constructed.

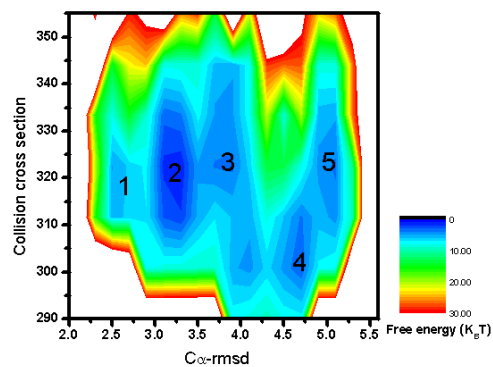
Integrated Tempering Sampling
molecular dynamics simulation (ITS-MDS)

AMBER

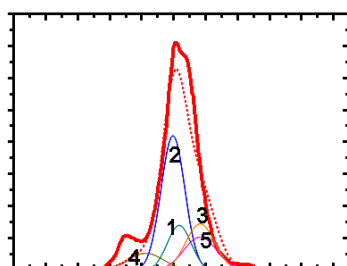
Free energy contour plot as a function of C α -rmsd and CCS



Weighting factor from the free energy profile
CCS calculation (MOBCAL)



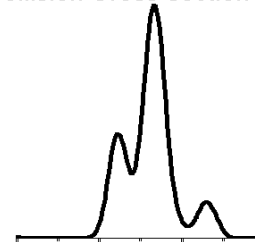
Theoretical Collision Cross-section profile



Predicted

Compare

IM Experimental Determined
Collision Cross-section profile



Measured

FIGURE 2. Method flow chart of utilizing ITS-MDS to interpret IMS data. Number 1 to 5 in the figure represent cluster numbers.

Hydrogen/Deuterium Exchange

In solution, labile hydrogens in peptides and proteins exchange with protons of the solvents. By changing to deuterated solvent, deuterium from the solvent will be incorporated in the labile hydrogen positions and the exchange reaction can be followed. Traditionally, NMR analysis has been applied to study hydrogen/deuterium exchange phenomena to gain insight into protein stability, protein dynamics.^{68,69} Mass spectrometry can also be used to monitor hydrogen/deuterium exchange process by measuring the mass increase as hydrogen is exchanged for deuterium. H/D exchange coupled to mass spectrometry has become a powerful analytical tool for the study of protein dynamics. In addition, combining data from other methods about protein dynamics, a more thorough understanding of protein structure/function can be obtained.⁷⁰

The relationship between measured H/D exchange rates and protein dynamics were described by Linderstrøm-Lang and colleagues.⁷¹ The H/D exchange rates depend primarily on pH, temperature, and how accessible to the deuterated solvent. There are generally two exchange mechanisms.^{72,73} If the rate of folding/unfolding is faster than the intrinsic amide exchange rate, this is known as the EX2 limit. On the other hand, if the folding/unfolding rate is slower than the rate of amide exchange, the EX1 limit is reached. If proteins follow EX1 mechanism, it would produce bimodal isotope pattern in the mass spectrum. The rate of H/D exchange at the EX1 limit would directly reflect the rate of the solvent exposure of the individual amide hydrogen. If the conformational

transitions occur between two states, EX1 exchange rate provides information about the kinetics of conformational interconversions.

H/D exchange coupled with mass spectrometry has also been combined with other mass spectrometry based techniques to gain insights of protein folding/unfolding dynamics problems. For example, Clemmer and coworkers have demonstrated previously that combining H/D exchange with IM separation to probe the ion mobility separated ubiquitin conformers in the gas-phase, which shows the potential of combining these two techniques together to explore the conformational space of biomolecules.⁷⁴ Chapter 5 will present a particular study in which solution phase H/D exchange is monitored by ESI-IM-MS to probe different conformer distributions of fast and slow exchange mass envelope.

CHAPTER III

GAS-PHASE CONFORMATIONS OF MODEL β -HAIRPIN PEPTIDE

TRYPTOPHAN ZIPPER 1

Introduction

Tryptophan Zipper 1 (trpzip1) (sequence: SWTWEGNKWTWK-NH₂), is a *de novo* designed peptide by Cochran *et al.*, which has been shown to favor a well-defined β -hairpin in solution.⁷⁵ β -hairpin is stabilized by tryptophan-tryptophan cross-strand pairs. Trpzip series of peptides (trpzip1 - 6), are minimal units of β tertiary structure, even for a short sequence (12 to 16 residues), have the thermodynamic properties of typical folded proteins. The stability of the hairpin was established by using circular dichroism, Raman and FT-IR spectroscopy.⁷⁶ Because of their small size, unusual stability, and very favorable spectroscopic properties, trpzip series of peptides have also been proven to be a good model system to study the folding of β -hairpins by several computational studies,⁷⁷⁻⁷⁹ specially ITS-MDS method.⁴⁰

In this study, ITS-MDS is used to derive candidate structures of a model peptide, Tryptophan Zipper 1 (trpzip1) and to predict the thermodynamics properties of candidate structures based on statistical sampling. The ITS-MDS data are then used to generate a hypothetical CCS profile that can be compared to experimental CCS profile.

*Reprinted with permission from “Molecular dynamics and ion mobility spectrometry study of model beta-Hairpin peptide, trpzip1” Chen, L.; Shao, Q.; Gao, Y.-Q; Russell, D. H. *J. Phys. Chem. A* 2011, 115, 4427-4435. Copyright 2011 by ACS Publications.

Gas phase IMS studies provide unique means of excluding solvent from affecting the overall stability of β -hairpin. In this study we use computational (ITS-MDS), experimental (IMS) and chemical derivatization (acetylation) to probe individual characteristic that influence structural preferences of trpzip1 and three modified (lysine acetylated) trpzip1 $[M + H]^+$ ions. The modified trpzip1 species are used to control the site of protonation and alter electrostatic intramolecular interactions. CCS profiles obtained from the ITS-MDS candidate structures are then compared to CCS profiles obtained from IMS.

Experimental Methods

Trpzip1 was custom synthesized by Genscript Corp. (Piscataway, NJ) and the modified (acetylated) peptide ions were purchased from GL Biochem (Shanghai, China). The purity of each of the four peptides was greater than 85%. The sequences and sites of acetylation of each peptide were confirmed by tandem mass spectrometry (Applied Biosystems 4700 Proteomics analyzer). The samples were prepared for MALDI by mixing peptide stock solution with α -cyano-4-hydroxycinnamic acid (Sigma Aldrich, St. Louis, MO) at 1000:1 matrix:analyte molar ratio.

The MALDI-IM-MS experiments were performed on a MALDI-IM-TOFMS that has been previously described.^{25,53} Briefly, the instrument consists of a drift cell coupled to a high-resolution reflectron time-of-flight (TOF) mass spectrometer. MALDI was performed using a frequency tripled Nd:YAG (355nm) laser (CrystaLaser, Reno, NV) operated at a pulse rate of 200 Hz. The MALDI ion source is maintained at a pressure of ~ 3 torr, and a potential of 1-2 volts is applied between the sample plate and skimmer

cone. Under these conditions the ions experience several hundreds of collisions prior to entering the ion mobility drift cell, thus the ion population entering the drift cell is equilibrated to the bath gas temperature of ~ 300 K. Although it is difficult to assess the temperature of the initially formed ion population owing to the fact that the exact mechanism of MALDI is not fully understood⁸⁰, there are distinct advantages to using MALDI for studies of peptide ion structure. Namely, the ions are initially formed with a distribution of internal energies, which allows the ions to sample a large volume of phase space, and the collisional cooling redistributes the ion population over the various potential energy minima that comprise the energy landscape.

The ion mobility drift tube length is 15 cm and maintained at a pressure ~ 3 torr He at room temperature (~ 300 K). All experimentally measured IM peak profiles were acquired at field strength of $E/P = 18 \text{ V cm}^{-1} \text{ torr}^{-1}$ ($E/N = 56 \text{ Td}$ at 298K). The ion drift times (t_d) used to obtain CCS were acquired under low-field conditions using six different field strengths to accurately calculate the mass-dependent drift time correction, t_0 ($t_{\text{ATD}} - t_0 = t_d$), which represents the time ions spend outside of the IM drift cell. CCSs were calculated using the empirical drift time (t_d) based on the hard sphere approximation:⁴¹

$$\Omega_{\text{avg}} = \frac{(18\pi)^{\frac{1}{2}}}{16} \frac{ze}{(k_b T)^{\frac{1}{2}}} \left(\frac{1}{m_i} + \frac{1}{m_B} \right)^{\frac{1}{2}} \frac{t_d E}{L} \frac{760}{P} \frac{T}{273.2} \frac{1}{N_0} \quad (6)$$

where z is the charge of the ion, e is elementary charge, k_b is Boltzmann's constant, m_i is the mass of the ion, m_B is the mass of buffer gas, E is the IM electric field strength, N_0 is

the number density of the drift gas at STP, L is the drift tube length, P is the buffer gas pressure and T is the system temperature. The mass spectrometer was externally calibrated using two-point calibration of the radical cations C_{60} ($m/z = 720$) and C_{70} ($m/z = 840$) (Sigma Aldrich, St. Louis, MO). The measurements of CCS were externally calibrated with bradykinin $[M + H]^+$ ions of 242 \AA^2 ($\pm 2\%$).²⁴ The 2D IM-MS data were acquired and processed by custom software (Ionwerks, Inc, Houston, TX).

The ESI-IM-MS data were acquired on a Synapt HDMS G2 mass spectrometer (Waters UK Ltd., Manchester, UK). CCS measurements were calibrated using tryptic digest peptides from cytochrome *c* and myoglobin according to the protocol developed by Ruotolo and coworkers.^{18,54} Literature values of CCS of calibrant peptides were taken from CCS database generated by Clemmer and coworkers.^{55,56} The samples were prepared for ESI in a 50:50 methanol/water mixture at a concentration of $2 \text{ }\mu\text{M}$. A variety of solvents were used (Methanol, 90:10 methanol/water, 50:50 methanol/water) and gave similar results, and the measured CCSs were independent of the solvent system.

Results and Discussion

ITS-MDS was carried out on six different forms of trpzip1 (amino acid sequence SWTWEGNK⁸WTWK¹²-NH₂), *i.e.*, three protonated forms of trpzip1, *viz.* $[M + H]^+$ ions where the N-terminus or lysine at position 8 (K⁸) or 12 (K¹²) is protonated, denoted H^+N , H^+K^8 , and H^+K^{12} respectively, and three acetylated forms of trpzip1, denoted H^+N -acK⁸K¹², H^+K^8 -acNK¹² H^+K^{12} -acNK⁸. The notation H^+K^8 -acNK¹² indicates protonation on the side chain of K⁸ and the N-terminus and K¹² are both acetylated (sequences

TABLE 1. The notation used to identify the derivatives of trpzip1, mass-to-charge ratios of the $[M + H]^+$ ions, experimental collision cross-sections (CCS) obtained by MALDI and ESI, calculated CCS values for the ions, and the percent γ -turn structure of the ion population. The notation H^+K^8 -acNK¹² indicates protonation on the side chain of K⁸ and both of the N-terminus and K¹² are acetylated.

| Name | Sequence | m/z ([M+H] ⁺) | Measured CCS (Å ²) | | Calculated CCS (Å ²) | % γ -turn |
|--|--|------------------------------|-----------------------------------|------------|-------------------------------------|------------------|
| | | | MALDI | ESI | | |
| H•N-acK⁸K¹² | (H•)SWTWEGNK(ac)WTWK(ac)-NH₂ | 1691.80 | 330 | 339 | 331 | 0 |
| H•K⁸-acNK¹² | Ac-SWTWEGNK(H•)WTWK(ac)-NH₂ | 1691.80 | 333 | 341 | 333 | 38 |
| H•K¹²-acNK⁸ | Ac-SWTWEGNK(ac)WTWK(H•)-NH₂ | 1691.80 | 328 | 337 | 326 | 25 |
| H•N | (H•)SWTWEGNKWTWK-NH₂ | 1607.78 | N/A | | 321 | 5 |
| H•K⁸ | SWTWEGNK(H•)WTWK-NH₂ | 1607.78 | N/A | | 318 | 0 |
| H•K¹² | SWTWEGNKWTWK(H•)-NH₂ | 1607.78 | N/A | | 321 | 47 |

shown in Table 1). Our objective is to use ITS-MDS to derive candidate structures on the basis of charge site under conditions where the effects of competing intramolecular interactions are controlled. It is important to note that ITS-MDS can be used to access the lowest energy structure as well as to generate the whole conformational space of the molecule of interest. Figure 3(A) displays the free energy maps obtained from ITS-MDS for the six distinct tripzip1 species, where energy is plotted as a function of CCS and backbone C α -rmsd. For comparison the free energy profiles for each species are shown in Figure 3(B). Backbone C α -rmsd values are calculated with respect to the structure closest to the ‘native’ trpzip1 (Protein Data Bank ID 1LE0) as a reference for each individual molecule. Although the reference structure for each case may differ, conformations within the lower C α -rmsd range (C α -rmsd < 2Å) closely resemble the native β -hairpin structure, while conformations within higher C α -rmsd range (C α -rmsd > 2Å) are very different from the native-like state. The lowest free energy regions are located at (C α -rmsd, CCS) = (3.25 Å, 320 Å²) for H⁺N, (3.23 Å, 323 Å²) for H⁺K⁸, (0.85 Å, 317 Å²) for H⁺K¹², (3.26 Å, 332 Å²) for H⁺N-acK⁸K¹², (0.57 Å, 331 Å²) for H⁺K⁸-acNK¹², (3.51 Å, 328 Å²) for H⁺K¹²-acNK⁸, respectively. The free energy maps (Figure 3A) of H⁺N and H⁺N-acK⁸K¹² both have global minima (located at 2.5 Å < C α -rmsd < 4 Å); conversely, the free energy maps for H⁺K⁸, H⁺K⁸-acNK¹², H⁺K¹² and H⁺K¹²-acNK⁸ contain multiple minima with relatively small energy barriers separating each. The highest free energy barrier for each molecule shown in Figure 3 (B) appears to be the energy barrier separating the native-like state and the highly disordered state. These energy barriers

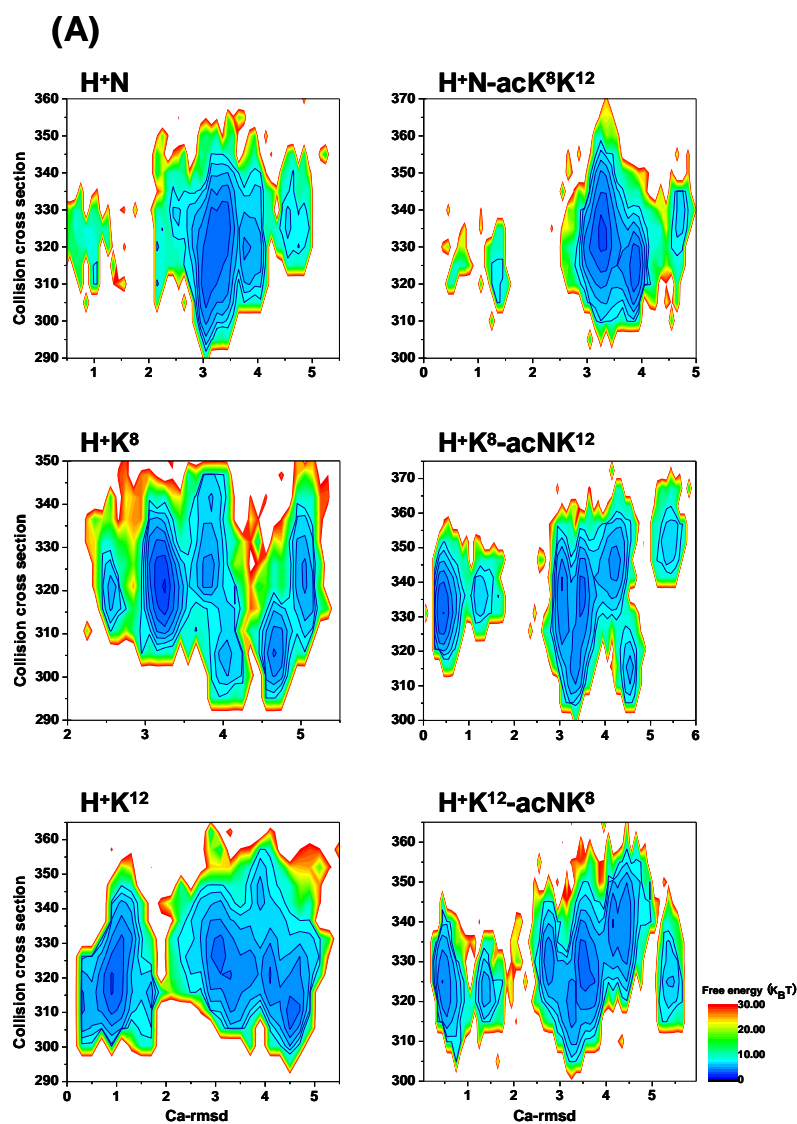


FIGURE 3. (A) The ITS-MDS free energy contour maps for each of the trpzip1 and its derivatives $[M + H]^+$ ions plotted as a function of backbone Ca -rmsd and collision cross-section (CCS). The interval between contour lines is $k_B T$. (B) A 2-dimensional cross section or free energy profile representation of part (A).

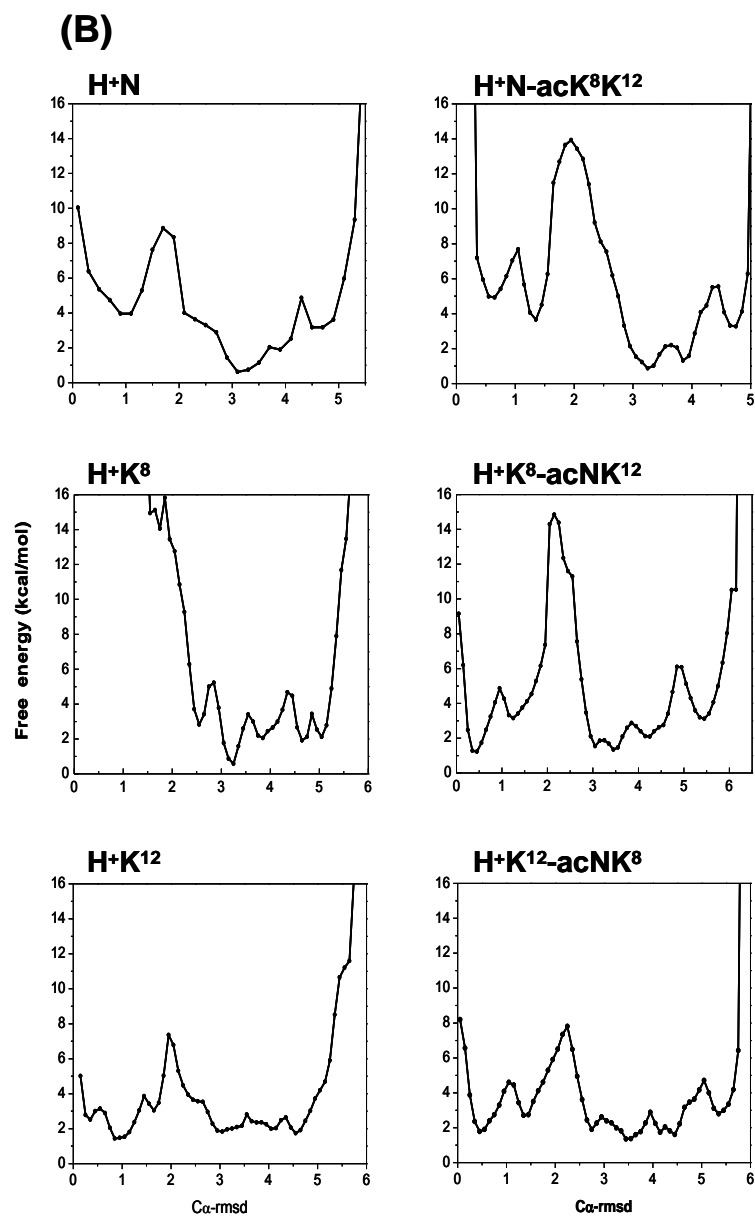


FIGURE 3. continued

range from ~15 kcal/mol for H^+K^8 -acNK¹² to as low as 6 kcal/mol for H^+N and H^+N -acK⁸K¹².

Cluster analysis was used to classify the populated conformations within each energy minimum in terms of the C α -rmsd between structures. Representative structures and the relative abundances of the most populated cluster are contained in Figure 4. Although solution phase studies suggest that trpzip1 has a well-defined type II' β -hairpin structure (sequence EGNK⁸) flanked by the sequence WTW, similar structures are not found among the solvent-free candidate structures obtained using ITS-MDS. Instead, ITS-MDS reveals structures with stable γ -turn at EGN for H^+N , H^+K^{12} , H^+K^8 -acNK¹² and H^+K^{12} -acNK⁸; specifically cluster1 of H^+N , clusters 1 and 2 of H^+K^{12} , cluster 1 of H^+K^8 -acNK¹² and clusters 1 and 2 of H^+K^{12} -acNK⁸ (see Figure 4; criteria used to define the β -turn and γ -turn⁸¹ are provide in the figure caption). The γ -turn structures range from 0% for H^+K^8 and H^+N -acK⁸K¹² to 47% for H^+K^{12} , with the other systems having relative abundances of 5% for H^+N , 38% for H^+K^8 -acNK¹², and 25% for H^+K^{12} -acNK⁸, see Table 1. Figure 5 compares the backbone structures of “native” trpzip1 (Protein Data Bank ID 1LE0) and the γ -turn structures for H^+N and for H^+K^8 -acNK¹² obtained from ITS-MDS. These two γ -turn structures have a C=O---H-N hydrogen bond between the amide oxygen of E⁵ and amide N⁷, whereas the two strands of the peptide backbone appear to be relatively straight owing to backbone-to-backbone hydrogen bonds between the two strands, specifically the side carboxylic acid group of E⁵ and keto group of N⁷, as well as the oxygen side chain of T³ and hydrogen T¹⁰.


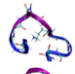
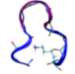

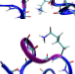
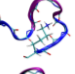


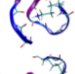

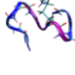
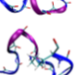
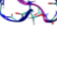

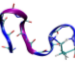
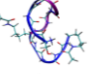

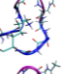
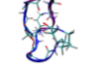
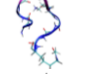

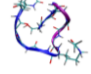
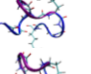
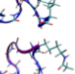
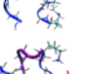
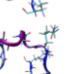

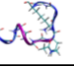

| (A) H ⁺ N | | | | (C) H ⁺ K ⁸ | | | | (E) H ⁺ K ¹² | | | |
|---|----------------------------|-----|--|---|----------------------------|-----|---|---|----------------------------|-----|---|
| Cluster | RMSD CCS Å ² | % | Representative structure | Cluster | RMSD CCS Å ² | % | Representative structure | Cluster | RMSD CCS Å ² | % | Representative structure |
| 1 | 0.35 328±10 | 5% |  | 1 | 3.23 323±7 | 59% |  | 1 | 0.85 317±7 | 40% |  |
| 2 | 3.08 330±9 | 5% |  | 2 | 3.74 327±8 | 7% |  | 2 | 3.08 327±10 | 7% |  |
| 3 | 3.42 323±8 | 14% |  | 3 | 4.02 308±7 | 8% |  | 3 | 3.51 315±6 | 7% |  |
| 4 | 3.83 321±10 | 14% |  | 4 | 4.66 307±6 | 8% |  | 4 | 3.88 340±12 | 4% |  |
| 5 | 4.61 327±8 | 5% |  | 5 | 5.01 323±7 | 5% |  | 5 | 4.02 318±6 | 5% |  |
| (B) H ⁺ N-AcK ⁸ K ¹² | | | | (D) H ⁺ K ⁸ -AcNK ¹² | | | | (F) H ⁺ K ¹² -AcNK ⁸ | | | |
| Cluster | RMSD CCS Å ² | % | Representative structure | Cluster | RMSD CCS Å ² | % | Representative structure | Cluster | RMSD CCS Å ² | % | Representative structure |
| 1 | 2.99 327±8 | 46% |  | 1 | 0.57 331±10 | 36% |  | 1 | 0.56 325±8 | 17% |  |
| 2 | 3.29 335±8 | 15% |  | 2 | 3.11 339±9 | 12% |  | 2 | 1.32 324±8 | 4% |  |
| 3 | 3.92 327±7 | 15% |  | 3 | 3.26 318±7 | 7% |  | 3 | 3.25 317±7 | 6% |  |
| | | | | 4 | 3.44 334±8 | 12% |  | 4 | 3.46 334±8 | 16% |  |
| | | | | 5 | 4.15 344±8 | 15% |  | 5 | 3.71 326±7 | 14% |  |
| | | | | | | | | 6 | 4.51 346±12 | 15% |  |

FIGURE 4. Structural representation for most abundant clusters for H⁺N (A), H⁺N-acK⁸K¹² (B), H⁺K⁸ (C), H⁺K⁸-acNK¹² (D), H⁺K¹² (E), and H⁺K¹²-acNK⁸ (F). The turn region EGNK⁸ is shown in purple. The protonated sites and all backbone atoms are shown in cylinder representation. The relative abundances (%) clusters that exceed 4% are shown.

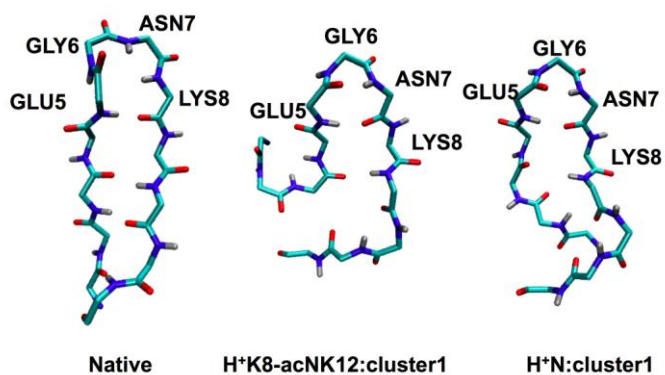


FIGURE 5. The native-like γ -turn structures found in the simulation: cluster1 of H^+K^8 -acNK¹² and cluster1 of H^+N . The native folded β -turn structure is also shown for comparison. The relative abundances for cluster1 of H^+K^8 -acNK¹² and cluster 1 of H^+N are 36% and 5%, respectively. The criteria used to define the β -turn is formation of hydrogen bond between the backbone C=O at position i and the N-H groups at position $i + 3$ or a distance of $\sim 7\text{\AA}$ between the C α at position i and C α at position $i + 3$. The γ -turn structure is defined by hydrogen bonding between the backbone C=O (i) and the N-H ($i + 2$).

The influence of electrostatic forces as a result of protonation at the N-terminus, K^8 or K^{12} on the gas-phase conformation of trpzip1 is further demonstrated by close inspection of the three different forms of singly protonated trpzip1 (H^+N , H^+K^8 and H^+K^{12}). Representative structures comprising the most populated clusters for H^+N/H^+N -Ac K^8K^{12} , H^+K^8/H^+K^8 -AcNK 12 , and H^+K^{12}/H^+K^{12} -AcNK 8 are shown in Figure 6. The γ -turn structure is present in H^+K^{12} (Figure 6(E)), but not in H^+N and H^+K^8 (Figure 6(C)), which suggest that protonation at sites near EGNK 8 reduces the probability for turn formation. Conversely, protonation on K^{12} (H^+K^{12}), which is remote from the turn region (EGNK 8) has no measureable effect on the γ -turn abundances. It appears that the protonated K^{12} is stabilized by cation- π interactions with the indole ring of W^4 (see the structure in Figure 6(E)).⁸² On the other hand, protonation on K^8 has a significant effect on the γ -turn structure owing to interactions of K^8 with the backbone carbonyl groups of W^2 , W^4 and N^7 (see the structure in Figure 6(C)), which favors formation of a random coil structure. Although the relative abundance of γ -turn structure for H^+N is quite low ($\sim 5\%$ in cluster 1; see Figure 4), the most populated cluster (cluster 3, see Figure 6(A)) of H^+N does not contain γ -turn structure, because the protonated N-terminus interacts with the backbone of C-terminal end and EGNK fails to form a turn. The structural differences seen for H^+N , H^+K^8 and H^+K^{12} demonstrate that electrostatic interactions arising from protonation greatly influence the solvent-free ion structures. That is, in a solvent-free environment, the protonated groups are stabilized by the intramolecular charge solvation of electronegative groups of the peptide.

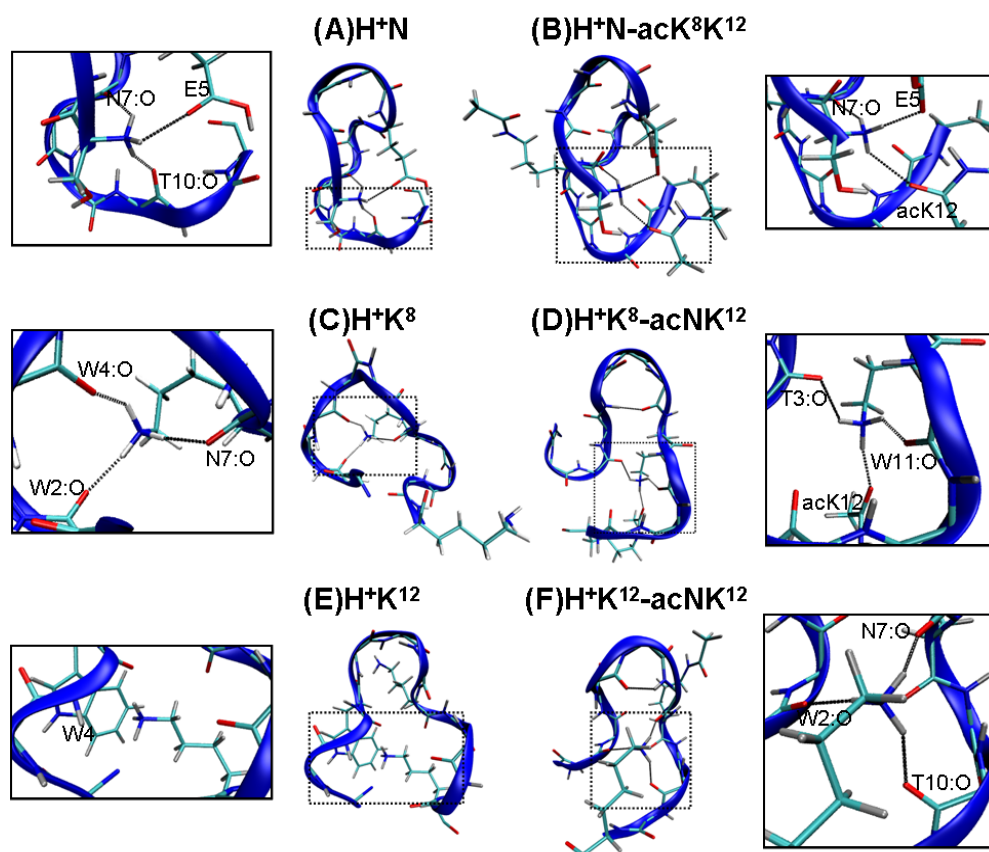


FIGURE 6. The structures of the most populated clusters for H^+N (A), H^+N -acK⁸K¹² (B), H^+K^8 (C), H^+K^8 -acNK¹² (D), H^+K^{12} (E), and H^+K^{12} -acNK⁸ (F), and an enlarged view of the structures show the intramolecular interactions that stabilize each structural form for each molecule. The protonated sites, all backbone atoms and all atoms H-bonded to the proton are shown in cylinder representation, and dashed lines represent H-bonds. Atoms or groups involved in intramolecular interactions are labeled. For example, the notation W4:O indicates the backbone carbonyl oxygen of residue W⁴ and the notation E5 indicates the side chain of E⁵.

Although the site of protonation has a strong influence on the overall energy landscape of gas phase peptide ions, it is also important to evaluate the effects of proton bridges (interactions between the K side chains; $\text{-NH}_2\text{---H}^+\text{---H}_2\text{N-}$) and salt-bridges ($\text{-COO}^-\text{---H}_3\text{N}^+\text{-}$) that may also influence the peptide ion conformation. Comparisons of three pairs of non-acetylated and acetylated derivatives (H^+N and $\text{H}^+\text{N-acK}^8\text{K}^{12}$, H^+K^8 and $\text{H}^+\text{K}^8\text{-acNK}^{12}$, H^+K^{12} and $\text{H}^+\text{K}^{12}\text{-acNK}^8$), where each of the pairs have the same protonation sites but secondary effects involving the non-acetylated lysine residue are changed owing to the lower proton affinity of the acetylated form. For H^+N and $\text{H}^+\text{N-acK}^8\text{K}^{12}$, the protonated N-terminus is solvated by the backbone and the acetylated K^8 and K^{12} ions has little effect on the conformation. As a consequence, H^+N and $\text{H}^+\text{N-acK}^8\text{K}^{12}$ both present a single free energy well with very similar populated clusters. In the case of H^+K^{12} and $\text{H}^+\text{K}^{12}\text{-acNK}^8$, cluster 1 of H^+K^{12} (population percentage: 40%) and clusters 1, 2 and 3 (population percentage: 17%, 4%, and 4% respectively) of $\text{H}^+\text{K}^{12}\text{-acNK}^8$ all contain similar γ -turn structure in the region of EGNK^8 . On the other hand, the representative structure for the most populated cluster for H^+K^8 (cluster 2; 59%) and $\text{H}^+\text{K}^8\text{-acNK}^{12}$ (Cluster 1; 36%) are quite different (see Figure 4 (C, D)). H^+K^8 and $\text{H}^+\text{K}^8\text{-acNK}^{12}$ have the same protonation site (K^8), but the protonated side chain (-NH_3^+) of H^+K^8 appear to be charge-solvated by the amide groups near the N-terminus (see the structure in Figure 6 (C)), while the protonated lysine side chain of $\text{H}^+\text{K}^8\text{-acNK}^{12}$ interacts with the amide group of acetylated K^{12} (see the structure in Figure 6 (D)). Such structural differences between non-acetylated and acetylated derivatives are also reflected in the overall topography of free energy maps. For example, the populated

clusters of H^+K^8 and H^+K^8 -acNK¹² differ significantly, while the free energy maps for H^+K^8 and H^+K^8 -acNK¹² are quite different.

The candidate structures and their fractional populations found by using ITS-MDS can be used to compute a hypothetical IMS CCS profile. That is, the relative abundances of the individual clusters dictates CCS profile and this data can be used to test the validity of the computations by comparing the computed and measured CCS profiles. The experimentally measured CCS profiles for three acetylated derivatives of trpzip1 (H^+N -acK⁸K¹², H^+K^8 -acNK¹², and H^+K^{12} -acNK⁸) are compared with the corresponding computed CCS profiles in Figure 7. The calculated CCS profiles of populated clusters (only clusters whose population above 4% are taken in consideration) of each molecule are also plotted in Figure 7. The centroid value of each cluster as well as the relative population of each cluster obtained by ITS-MDS is critical for the calculation fit to the experimentally measured CCS profile. For all three acetylated derivatives, the CCS profile derived from summing the populated clusters (dotted lines in Figure 7) matches well with the experimentally measured CCS profile, which indicates that ITS-MDS provides an accurate estimate of the free energy of each cluster group which in turn accurately predict the CCS profile from calculation.

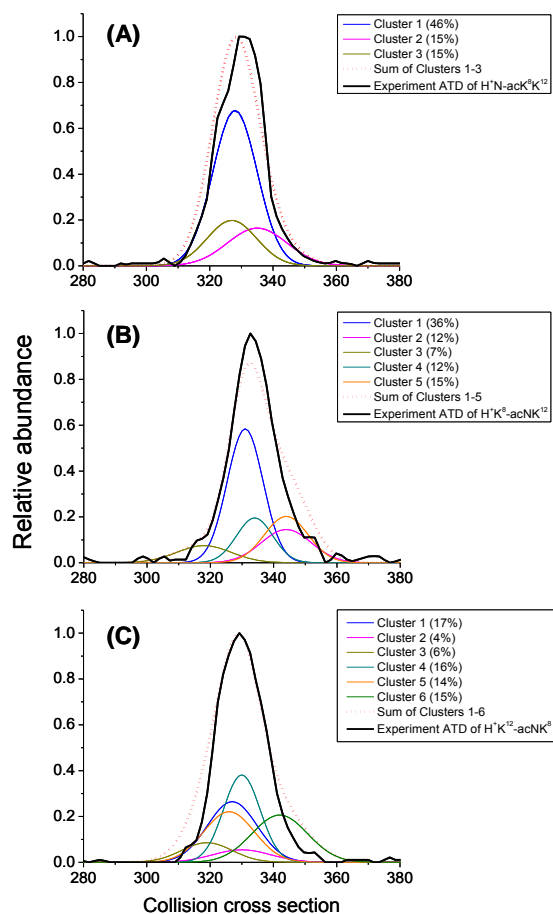


FIGURE 7. Plots of collision cross-section (CCS) profiles for three acetylated derivatives of trpzip1, $H^+N\text{-ac}K^8K^{12}$ (A), $H^+K^8\text{-ac}NK^{12}$ (B), and $H^+K^{12}\text{-ac}NK^8$ (C). The CCS profiles for the most populated clusters for each molecule are also shown in color. The dotted line represents the sum of the CCS profiles of the most populated clusters. This data only includes structures that exceed 4% relative abundances.

Computed and experimental CCS profiles of non-acetylated trpzip1 $[M + H]^+$ ions are contained in Figure 7. Trpzip1 has three potential protonation sites, *viz.* N-terminus, K⁸ and K¹², thus the ion population could be a mixture of isomers of $[M + H]^+$ ions of H⁺N, H⁺K⁸, and H⁺K¹², which differ only in terms of site of protonation and the resulting intramolecular interactions.⁸³ The ratio of H⁺N, H⁺K⁸, and H⁺K¹² (1:8:24) was determined by fitting the experimentally determined CCS profile of trpzip1 $[M + H]^+$ ions using an ensemble of the calculated CCS profiles (H⁺N, H⁺K⁸, and H⁺K¹²), which are also shown in Figure 8. If the rate of intramolecular proton transfer between the isomers is slow relative to the ion drift time, then the ratio of the three protonated isomers represent equilibrium values. Owing to the significant differences in proton affinities (PA) of lysine (~ 238 kcal mol⁻¹)⁸⁴ and the N-terminus (~ 212 kcal mol⁻¹)⁸⁴ the abundances of H⁺K⁸ and H⁺K¹² should be significantly higher than that for H⁺N. On the other hand, the ratio of H⁺K⁸:H⁺K¹² should depend on the relative basicities of the two lysine residues, which is influenced by the local environment and the specific structure, especially possible intramolecular interactions (charge-solvation) involving the protonated lysines. In addition, the possibility of forming a zwitterion of trpzip1 (protonated at K⁸ or K¹² and deprotonated at E⁵) was also considered. The predicated CCS profile for zwitterionic forms are much broader than the measured peak profile of trpzip1 $[M + H]^+$ ions suggesting that zwitterionic conformers are not present (data not shown).

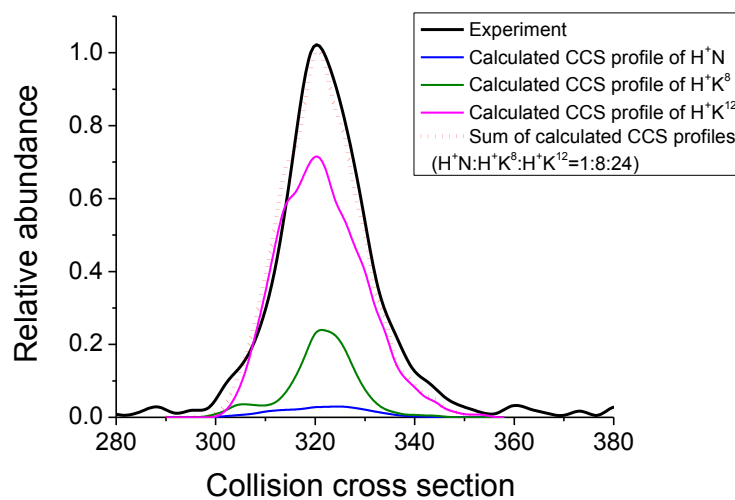


FIGURE 8. Experimental (solid line) and calculated best-fits (dotted line) for the CCS profiles of [Trpzip1 + H]⁺. The calculated collision cross-section profiles of H⁺N, H⁺K⁸, and H⁺K¹² are also shown. The estimated ratio of the population of H⁺N, H⁺K⁸, and H⁺K¹² is 1:8:24.

The peak centroids for the acetylated peptides CCS (H^+N -acK⁸K¹², H^+K^8 -acNK¹², and H^+K^{12} -acNK⁸) are larger than that for the non-acetylated counterparts (H^+N , H^+K^8 , and H^+K^{12}) by approximately 10 Å², and an increase in CCS of this magnitude agrees quite well with calculated CCS shown in Figure 8, giving confidence to the calculations. The centroid CCS data extracted from the CCS profiles in Figure 8 are also listed in Table 1. Note: for comparison CCS data obtained by using electrospray ionization are included in Table 1, and the small differences (~2-3%) in the measured values are not regarded as significant. Likewise, the ~3% increase in CCS upon addition of two acetyl groups suggest that globular-to-extended structural transition does not occur; typically CCS values for helices are 7-10% larger than that for globular structures.^{25,28} On the other hand, a detailed analysis of the free energy maps of the six molecules reveals that the overall topography of the non-acetylated and acetylated counterparts is quite different as described above.

Conclusions

Integrated tempering sampling-molecular dynamics simulations (ITS-MDS) combined with IMS is used to characterize the conformational space of a model β -hairpin peptide trpzp1 and three derivatives (acetylated lysine) of the peptide. The ITS-MDS approach yields CCS profiles as well as the free-energy landscapes. The calculated CCS profiles agree very well with the experimentally measured CCS profiles, which underscore the utility of the method for determining candidate structures as well as the relative abundances of the candidate structures. For example, ITS-MDS structural analysis suggests that γ -turn structures are preferred for unsolvated trpzp1 protonated

molecules, $[M + H]^+$ ions, rather than the β -turn structure that is preferred in solution.⁸ Differences in structural preferences for gas phase vs solution phase species are in agreement with prior results that suggest the secondary structure of the sequence EGNK⁸ depends on the environment.⁸¹ For example, glycine is known to have a high occupancy at position $(i + 1)$ of type II' β -turn in the condensed phase,⁸⁵ but gas phase studies using IR/UV double resonance spectroscopy and DFT quantum calculations suggest that γ -turn structures are favored over β structures.⁸¹ Similar observations were reported for the tripeptide Z-Aib-Pro-NHMe (Z=benzyloxycarbonyl), *i.e.*, a β -turn structure^{86,87} is favored in the condensed phase whereas the γ -turn structure is favored in the gas phase.⁸⁸

Although solvent plays an important role in defining the peptide/protein folding landscape, there is a balance between solvent, specific amino acid sequences and stabilizing intramolecular interactions, *i.e.*, salt-bridge formation, hydrophobic interactions, and non-bonding- π interactions. In an effort to separate solvent effects from these intrinsic parameters, computational studies are typically carried out using a variety of solvent models; however, studies of solvent-free peptides combined with chemical derivatization of specific functional groups also provides a means to decouple solvent effects from intramolecular electrostatic interactions. The influence of the electrostatic interactions arising from protonation and/or acetylation is reflected by the abundances of γ -turn structures for three protonated isomers, *i.e.*, H^+N , H^+K^8 , and H^+K^{12} as well as the three acetylated derivatives, *i.e.*, H^+N -acK⁸K¹², H^+K^8 -acNK¹², and H^+K^{12} -acNK⁸. That is, in a solvent-free environment, the protonated groups are stabilized by the intramolecular charge solvation of electronegative groups of the peptide. In the

absence of interactions between the protonation site and the turn region backbone, the γ -turn is more readily formed. Although the location of charge plays an important role in determining the gas-phase conformation, it is certainly not the sole factor. For example, the populated clusters of H^+K^8 and $\text{H}^+\text{K}^8\text{-acNK}^{12}$ differ significantly, even though H^+K^8 and $\text{H}^+\text{K}^8\text{-acNK}^{12}$ have the same (K^8) protonation site.

Previous studies suggest that helices are favored for gas phase protonated ($[\text{M} + \text{H}]^+$) or Na^+ adduct ions ($[\text{M} + \text{Na}]^+$) when the charge is near the C-terminus, owing to charge alignment with the helix macrodipole^{89,90}; however, very low abundances ($\sim 4\%$) of helix-like structures are observed for H^+K^{12} and H^+K^8 ions. In both cases it appears that the charge center interacts with the C-terminus of the molecule to promote helix formation. The population differences are the result of the protonation of H^+K^{12} , which is closer to the C-terminus and can readily aligned with the helix dipole. A similar result was reported for IRMPD and MD/DFT calculations for the gas phase Ac-VQIVYK-NH₂ ions, *i.e.*, the authors suggested that protonation of the lysine side-chain induces a transition from a β -hairpin-like structure to a helical structure as a result of alignment of the helix dipole.⁹¹ For trpzip1 ions the interconversion of a β -hairpin to helix appears to be less favored owing to the preferences for forming γ -turn structures.

CHAPTER IV

THE EFFECT OF ALKALI METAL ION BINDING ON CONFORMATIONS OF GRAMICIDIN A

Introduction

Ion transport across biological membranes is an important cellular process that is influenced by the composition of the lipid membrane as well as conformation and state (monomer or multimer) of the membrane interacting peptide or protein. Previous studies have shown that the dimer of gramicidin A (GA), a naturally occurring pentadecapeptide from *Bacillus brevis*, forms monovalent specific ion channels in lipid membranes; however, the monomer of GA is highly flexible and conformer preferences depend on solvent, concentration and temperature. The conformer preferences of both GA dimers and monomers are attributed to the hydrophobicity of the molecule. The amino acid sequence is composed entirely of aliphatic and aromatic amino acids and the protected N-terminus (formylated) and C-terminus (ethanolamide): HCO-Val-Gly-Ala-DLeu-Ala-DVal-Val-DVal-Trp-DLeu-Trp-DLeu-Trp-DLeu-Trp-NHCH₂CH₂OH. The self-assembly of GA resulting in formation of membrane pores is facilitated by the alternating sequence of D- and L-amino acids. Owing to its biological importance and high structural flexibility the conformation of GA in the condensed phase has been studied

*Reprinted with permission from “How alkali metal ion binding alters the conformation preferences of gramicidin A: A molecular dynamics and ion mobility study” Chen, L.; Gao, Y. Q; Russell, D. H. *J. Phys. Chem. A* 2012, 116, 689-696. Copyright 2012 by ACS Publications.

using both experimental⁹²⁻⁹⁶ and computational techniques.^{97,98}

Similar to the GA monomer, GA dimers form various conformations that depend on the solvent, peptide concentration, and temperature.^{93,99,100} For example, in alcohol solutions, GA dimers adopt double-stranded helices,^{94,100} whereas in more polar solvents such as H₂O, dimethyl sulfoxide and 2,2,2-trifluoroethanol, GA exists predominantly in monomer form.⁹⁴ In the solid phase, GA also exists in various forms; the crystal structure of ion-free GA and cesium-bound GA are both left-handed anti-parallel double helices, but each form has different numbers of residues per turn, which yield quite different pore diameters. The conformation for the Cs⁺-bound form has 7.2 residues per turn¹⁰¹ whereas the ion-free form has 5.6 residues per turn.¹⁰² Although the structure of the GA dimer has been extensively studied, the structure of the monomer and the mechanism by which monomers assemble to form dimers are not fully understood.

The high degree of structural flexibility of GA in the condensed phase makes it an excellent test case for critically evaluating enhanced sampling MDS as a predictive computational technique for interpretation of IMS data. In this paper, ITS-MDS is used to generate a population of gas phase conformers, as well as the abundances and free-energies of each conformer, which is then used to generate a theoretical CCS profile that can be compared with the experimental CCS profile.²¹ Good agreement between theoretical and experimental CCS profiles increases the level of confidence for conformation assignments from IMS data as opposed to making comparisons of IMS data to structure predictions that are based on other techniques, *i.e.*, small-angle X-ray scattering, X-ray diffraction and/or multi-nuclear NMR.^{21,31}

Here, we employ ITS-MDS to investigate the conformational preference of neutral GA as well as alkali metal ion adducts of GA, denoted $[GA + \text{met}]^+$ (met = Na, K, or Cs) and compare the predicted conformations of $[GA + \text{met}]^+$ with collision cross-section (CCS) profiles obtained by using electrospray ionization (ESI)-ion mobility (IM) experiments. Each experimentally determined CCS profile for alkali metal ion adducts of GA has distinct and unique features. ITS-MDS for neutral GA and the alkali metal ion adducts provide a detailed exploration of conformational space yielding new insights about how the binding of metal ions influences the intrinsic conformations of GA as well as how the conformations of the metalated GA change for different metal ion binding.

Experimental Methods

Integrated tempering sampling molecular dynamics simulation (ITS-MDS) is employed to enhance conformational sampling of polypeptide conformation space,^{37,38,40} and the use ITS-MDS for interpretation of IMS data was previously described.^{21,31} Briefly, a suitable bias potential is applied to the potential energy surface of the real system to enable sufficient samplings of a wide energy range. The bias potential consists of a series of Gaussian functions. Thermodynamic properties of the system are calculated by using recovered probabilities through a weighting factor yields in ITS-MDS.

MD simulations were performed using the AMBER 9.0 package. The AMBER FF99SB all-atom force field was used for all amino acid residues. MD simulations were performed *in vacuo* at 300K by using the weak-coupling algorithm with a coupling constant of 5.0 ps^{-1} and no non-bonded cutoff was used in simulations. First, short

simulations were run at the desired temperature 300 K to define the energy range to be explored and an iterative procedure is then used to determine a bias potential. Finally, six independent MD simulation trajectories were obtained using the bias potential with a length of 300 ns were obtained. Each trajectory starts from a randomly generated initial structure, and for the metal-peptide adducts, the locations of metal ions are also randomized.

Collision cross-sections for candidate conformations generated by ITS-MDS were calculated using the trajectory method in the MOBCAL software. The calculated collision cross section (see Figure 9) is assigned as the trajectory method value. Lennard-Jones pair potential parameters for Cs-He atom pair used in the trajectory method were taken from Fernandez-Lima et al.¹⁰³ The candidate conformations were clustered (using AMBER MMTSB tool set)⁶⁷ on the basis of similarities between backbone C α root-mean-square deviation (C α -RMSD); the cluster radius was arbitrarily selected as 3 Å. This method is similar to that described previously by Tao et al.³² The CCS calculations were conducted on conformations that fall within +/- 1 Å of the centroid conformation. Calculated cross section profiles were generated based on the thermodynamic distribution determined in MD simulation, and the free energy map was calculated as a function of potential energy and C α -RMSD.

Gramicidin A (HCO-Val-Gly-Ala-DLeu-Ala-DVal-Val-DVal-Trp-DLeu-Trp-DLeu-Trp-DLeu-Trp-NHCH₂CH₂OH) was purchased from Sigma-Aldrich (St. Louis, MO) and used without further purification. Stock solutions containing 1mM amounts of GA were prepared by dissolving the peptide in different solvents (methanol, ethanol,

propanol, and 50:50 (v/v) methanol:H₂O). Metal ion peptide adducts were formed by adding a metal chloride salt at a metal salt concentration of 5 mM into the peptide stock solution. The resulting metalated GA solution was diluted to ~2 μ M concentration of GA for analysis by electrospray ionization-ion mobility-mass spectrometry (ESI-IM-MS).

Des-formyl GA was prepared according to the procedure described previously.¹⁰⁴ Briefly, a stock solution of GA was prepared by dissolving 1 mg peptide in 1 mL of ethanol. The reaction mixture was prepared by mixing 100 μ L of peptide stock solution with 1 mL of 2M hydrochloric acid. The reaction was allowed to proceed for a period of 2 hours at room temperature. The sample was dried by lyophilization. The peptide solution was reconstituted in 100 μ L ethanol and analyzed by mass spectrometry without further purification.

The ESI-IM-MS data were acquired on a Waters SynaptTM HDMS G2 mass spectrometer (Waters UK Ltd., Manchester, UK) equipped with a travelling-wave ion mobility cell maintained at 3 mbar of nitrogen. Ions were formed by nano-ESI using a source temperature of ~100 °C and capillary voltage 1.6-2.2 kV. A range of cone and the extraction voltages 5-100 V and 1-4 V, respectively, were used in the experiments (see below). For the IM experiments, the traveling wave ion mobility cell was operated at wave velocity of 550 m/s and wave amplitude of 38 V. Collision cross section (CCS) calibration was performed using methods described previously by Ruotolo et al.^{18,54} Calibration standards included tryptic digest peptides from cytochrome *c* and myoglobin.

Literature values of CCS of calibrant peptides were taken from CCS database generated by Clemmer and coworkers.^{55,56}

It is important to note that the drift time profiles of different metal bound forms were insensitive to the solvent. In addition, the effect of source/cone voltages and kinetic energy of ions entering the ion mobility drift region were examined. The drift time profiles were unchanged regardless of the solvent conditions or the voltages applied, which suggests that the conformations represent gas phase conformations.

Results and Discussion

For most peptides the charge carrying site(s) can be estimated on the basis of proton or metal ion affinities of the amino acid side chains and the N- and C-termini; however, GA does not contain any basic or acidic side chains and both the N- and C-termini are protected. In an effort to understand the effects of alkali metal ion binding on the conformation of GA, it is important to first characterize the conformer preferences of neutral, metal-free GA. Thus, ITS-MDS was used to generate candidate structures dictated solely by the amino acid sequence. Next ITS-MDS was used to predict conformations, relative abundance and free energies for the alkali metal ion adducts of GA using ITS-MDS, which are compared to similar data obtained from ion mobility experiments.

ITS-MDS was performed on neutral GA *in vacuo*. The simulations yielded eight distinct conformer clusters having abundances that exceed 5% (see Figure 9). The simulation suggests a high β -sheet-forming tendency throughout the entire sequence, which includes several β -helix/ β -helix-like conformations found for lower energy states,

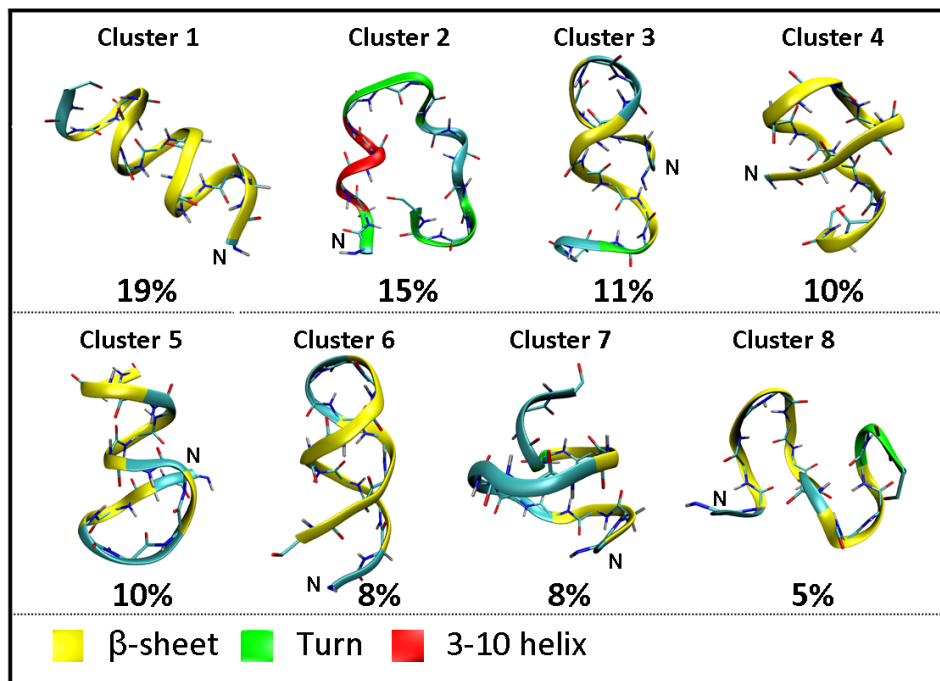


FIGURE 9. ITS-MDS derived conformations for neutral gramicidin A *in vacuo*. The population of each conformer is shown in the figure. Only clusters that exceed 5% relative abundance of the total population are shown. Position of N-terminus is labeled as 'N'. The backbone is shown in ribbon representations. All backbone atoms are shown in cylinder representations. Secondary structures are color-coded as shown in the figure. Yellow represents β -sheet. Green represents turn. Red represents 3-10 helix.

viz. right-handed $\beta^{4,4}$ -helix (cluster 1, 19%), left-handed $\beta^{4,4}$ -helix-like (cluster 5, 10%), right-handed $\beta^{6,3}$ -helix-like (cluster 7, 8%), and monomeric double-stranded β -helix (cluster 6, 8%). Other conformers that were found include β -hairpin-like (cluster 8, 5%), misfolded double-stranded β -helix (cluster 3, 11%) and random coil with short α -helix (cluster 2, 15%).

Two well-defined β -helix structures were found by simulation. Cluster 1 is a single strand right-handed $\beta^{4,4}$ -helix, containing nine hydrogen bonds between the backbone amide oxygen atom of residue n and amide hydrogen of residue $n + 5$ ($n = 2, 4, 6, 8$), and between the backbone amide hydrogen of residue m and amide oxygen atom residue $m + 3$ ($m = 2, 4, 6, 8, 10$). Cluster 6 (8%) is an ordered monomeric double β -helix structure that appears to be very similar to the anti-parallel double helix that has been suggested from previous solution phase studies.^{94,100} This conformer contains nine backbone hydrogen bonds between Gly²:NH-Leu¹⁴:CO, Gly²:CO-Leu¹⁴:NH, Leu⁴:NH-Leu¹²:CO, Leu⁴:CO-Leu¹²:NH, Val⁷:NH-Trp¹³:CO, Val⁷:CO-Trp¹³:NH, Trp⁹:NH-Trp¹¹:CO, Trp⁹:NH-Trp¹¹:CO, Val⁶:NH-Leu¹⁰:CO. The differences between the single strand $\beta^{4,4}$ -helix (cluster 1) and monomeric double helix (cluster 6) is the residue specific stabilizing hydrogen bonds formed between two chains in the dimeric form.

Two unusual patterns of hydrogen bonding networks in cluster 1 and cluster 6 of neutral GA are attributed to D, L-amino acid alternating sequence, which enables all of the side chains to protrude from the same side of the β -sheet. Such conformers differ significantly from conformers found in peptides containing all L-amino acids where adjacent side chains arrange themselves on opposite sides of the sheet. This important

structural feature is essential for ion channel forming peptides such as GA, allowing GA to fold into a β -helix with hydrophobic side chains of residues to be exposed to the outside of helix, thereby projecting the hydrophilic peptide backbone to form the interior of the pore and allow ion passage.

The free energy landscape as a function of the potential energy of the system and C α -RMSD is shown in Figure 10; note the large free energy barrier (Figure 10B) between cluster 1 and clusters 2-8. Cluster 1 is separated from the remaining clusters (2-8) by a high energy because structural transition is associated with disrupting the well-organized backbone hydrogen bonding network characteristic of helices. Such rearrangements would be highly unfavorable in low dielectric environments (*in vacuo* or in membranes) where electrostatic interactions are greatly enhanced.¹⁰⁵ It appears (see Figure 10) that cluster 1 represents the lowest free energy conformer of GA. Although cluster 8 has the lowest potential energy ($\sim 30 \text{ kcal}\cdot\text{mol}^{-1}$), cluster 1 has the lowest free energy, which suggests that cluster 1 is entropically favored over cluster 8.

In spite of the large conformational differences between clusters 1-8, the relative abundance (free energy) of each conformer as indicated in Figure 9 is similar, implying considerable intrinsic structural flexibility of GA. The condensed phase conformation of GA is known to be highly dependent on the environment. For example, in lipid membranes GA shows a strong preference for head-to-head right-handed single-stranded $\beta^{6,3}$ -helical dimer,¹⁰⁶⁻¹⁰⁸ which is similar to the right-handed $\beta^{6,3}$ -helix-like (cluster 7, 8%) found in our simulation. Hinton suggested that GA forms right-handed $\beta^{4,4}$ -helix in

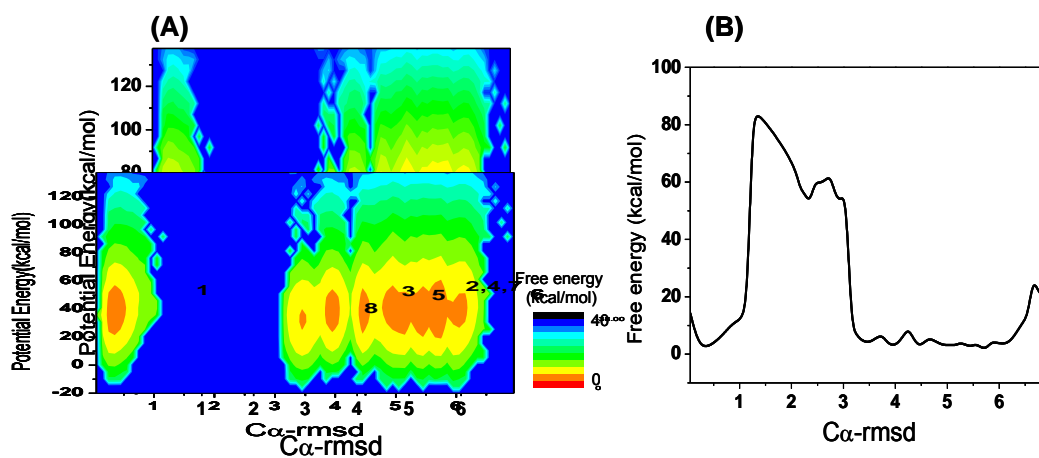


FIGURE 10. (A) The free energy landscape is plotted as a function of the potential energy and C α -RMSD for gramicidin A *in vacuo*. (B) Two-dimensional free energy profile representation of part (A). The number labeled in the figure corresponds to the cluster numbering used in Figure 9.

alcohol solution,¹⁰⁹ and this is the lowest free energy structure found by ITS-MDS. The preference of β -helix structure *in vacuo* is consistent with results of structures in low dielectric media. For example, interacting with lipid-like molecules, the preference of GA shifts towards specific conformers, such as $\beta^{6,3}$ -helix in the membrane.

The influence of an alkali metal ion on the conformer preferences of monomeric GA was studied using ITS-MDS on GA monomer coordinated by alkali metal ions (Na, K, Cs). The CCS and relative abundances for conformers representing the most populated clusters found by ITS-MDS are contained in Figure 11. It is interesting to note that the structural diversity of each of the alkali metal ion species as indicated by populations of conformers is quite different. For example, in the case of $[\text{GA} + \text{Na}]^+$ ions there are four major clusters having similar relative abundances, whereas for $[\text{GA} + \text{K}]^+$ and $[\text{GA} + \text{Cs}]^+$ ions the population is skewed toward a single dominant conformer (cluster1, 31%). However, it also important to note that for each ion form there is evidence for conformers that retain elements of the double-stranded β -helix as is the case for neutral GA.

Representative conformers for $[\text{GA} + \text{met}]^+$ (met = Na, K, or Cs) ions are shown in Figure 11. The coordination assignments (shown as black dash lines in Figure 11) are based on previously reported average interaction distances between the metal centers (Na^+ , K^+ , Cs^+) and the coordination sites.¹¹⁰ The average interaction distances calculated from candidate structures of $[\text{GA} + \text{Na}]^+$, $[\text{GA} + \text{K}]^+$ and $[\text{GA} + \text{Cs}]^+$ are $2.5 \pm 0.2 \text{ \AA}$, $2.8 \pm 0.1 \text{ \AA}$, and $3.1 \pm 0.1 \text{ \AA}$ respectively. In each case the alkali metal ion is coordinated by amide oxygen atoms; the exception is cluster 4 of $[\text{GA} + \text{Na}]^+$ ions that appears to be

stabilized by cation- π interaction with the Trp¹⁵ side chain. Although Na⁺ coordination by oxygen ligands are usually favored, cation- π interactions are quite common, especially in the case of Trp containing peptides/proteins.¹¹¹ The coordination number (CN) for most of the [GA + Na]⁺ and [GA + K]⁺ conformers is 6, but cluster 3 of [GA + Na]⁺ and cluster 2 of [GA + K]⁺ have CN of 5. In the case of [GA + Cs]⁺ the CN for cluster 1 is 6 but the other clusters also appear to have CN of 5. Although it seems reasonable to suggest that one open coordination site is an indication that the ion initially retained a solvent molecule, specifically H₂O, which was lost during the ESI process, there is no direct evidence to support this argument.

Alkali metal ions act as allosteric effectors for both peptides and proteins,¹¹² and they also alter conformer preferences of peptide/protein gas-phase ions. For example, [M + H]⁺ ions of polyalanine peptides favor a random globule, whereas α -helical conformers are favored for [M + Na]⁺ ions because the positive charged on the C-terminus aligns with the macrodipole;^{89,90,113} however, a similar effect is not operative for GA owing to the modified C-terminus. Thus, it is particularly interesting to note that the conformer preferences for [GA + Na]⁺ ion are similar to those for neutral GA. Superimposed conformers for four populated clusters of [GA + Na]⁺ with the corresponding neutral GA conformers are shown in Figure 12. The root-mean-square deviation (RMSD) for backbone C α atoms between neutral GA and [GA + Na]⁺ ions are in the range of 1.4 to 3.4 Å (see Figure 12). The preferred conformers for the metal bound peptides can be understood in terms of the balance between maximizing the metal

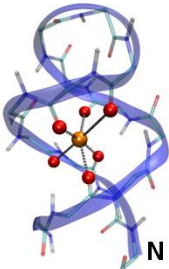
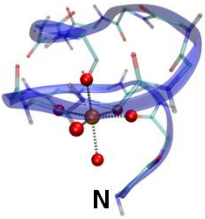
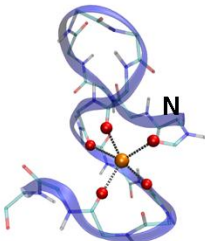
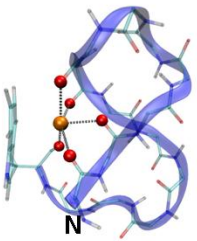
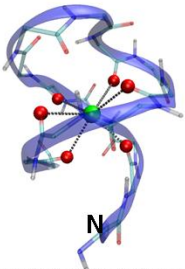
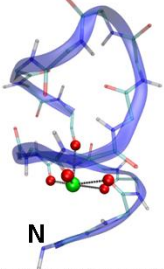
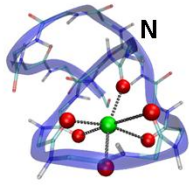
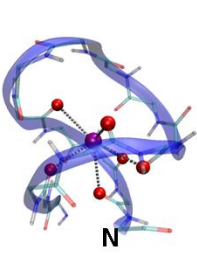
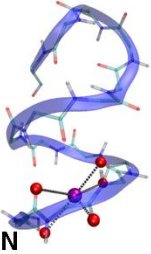
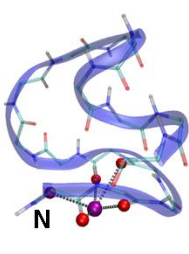
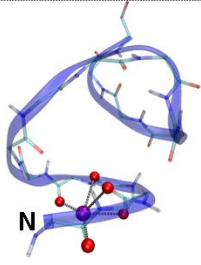
| | Cluster 1 | Cluster 2 | Cluster 3 | Cluster 4 |
|-----------------------------|--|--|---|--|
| $[\text{GA} + \text{Na}]^+$ |  |  |  |  |
| $[\text{GA} + \text{K}]^+$ |  |  |  | |
| $[\text{GA} + \text{Cs}]^+$ |  |  |  |  |
| | Cluster 1 | Cluster 2 | Cluster 3 | Cluster 4 |
| | CCS(\AA^2), %pop | CCS(\AA^2), %pop | CCS(\AA^2), %pop | CCS(\AA^2), %pop |
| $[\text{GA} + \text{Na}]^+$ | 408 \pm 9, 13 | 416 \pm 7, 8 | 419 \pm 7, 10 | 408 \pm 8, 12 |
| $[\text{GA} + \text{K}]^+$ | 393 \pm 6, 31 | 400 \pm 6, 9 | 413 \pm 8, 17 | — |
| $[\text{GA} + \text{Cs}]^+$ | 389 \pm 7, 31 | 405 \pm 8, 10 | 392 \pm 7, 13 | 402 \pm 8, 14 |

FIGURE 11. ITS-MDS derived conformations, calculated CCSs, and cluster relative abundances for $[\text{GA} + \text{Na}]^+$, $[\text{GA} + \text{K}]^+$, and $[\text{GA} + \text{Cs}]^+$. Only clusters that exceed 5% relative abundance of the total population are shown. All backbone atoms are shown in cylinder representation.

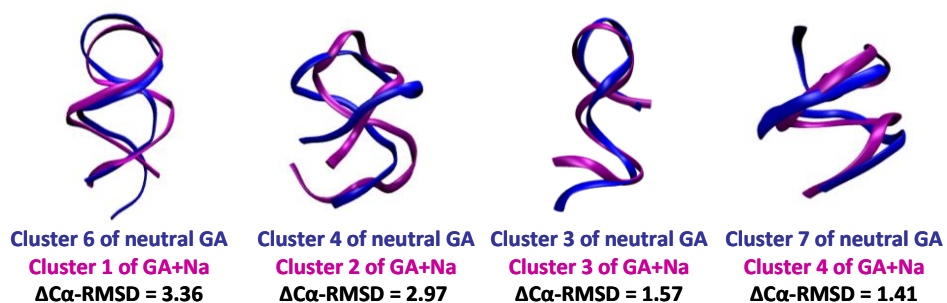


FIGURE 12. Backbone over-layed conformers of four clusters of $[GA + Na]^+$ ions with the corresponding neutral GA conformers. Magenta: $[GA + Na]^+$. Blue: neutral GA. The root-mean-square deviation (RMSD) for backbone $C\alpha$ atoms between $[GA + Na]^+$ and neutral GA are also shown.

coordination and minimizing the disruption to the native conformation. The close resemblances of conformers of neutral GA and $[\text{GA} + \text{Na}]^+$ ions suggests that the inherent conformations of neutral GA are able to accommodate the Na^+ ions without dramatically disrupting the native conformations.

As the metal size increases, the conformer preferences differ significantly from that for neutral GA. For example, the conformer of cluster 6 of neutral GA (see Figure 9), which is monomeric double β -helix, is very similar to cluster 1 for $[\text{GA} + \text{Na}]^+$ ions (see Figure 11). This is also true for cluster 1 of $[\text{GA} + \text{K}]^+$ and $[\text{GA} + \text{Cs}]^+$ ions. Note that the N- and C-termini are positioned in close proximity and the metal ion is positioned near the center of the molecule and coordinated by the amide backbone; however, the ‘pore’ along the double helix axis expands as metal ion size increases (Na^+ $0.97 \text{ \AA} < \text{K}^+$ $1.33 \text{ \AA} < \text{Cs}^+$ 1.67 \AA).¹¹⁴ That is, the double helix conformer of $[\text{GA} + \text{K}]^+$ is distorted relative to that of $[\text{GA} + \text{Na}]^+$ ions, and this distortion is even greater for $[\text{GA} + \text{Cs}]^+$ ions. Cluster 2 of each metal-GA complex (see Figure 11) appears to have evolved from single stranded β -helix such as clusters 1, 5, or 7 of neutral GA (see Figure 9). The metal ion binding sites in each case are near the N-terminus, which remain quite ordered, and the C-terminus of $[\text{GA} + \text{Na}]^+$ is also ordered ($\beta^6, ^3$ helix) owing to hydrogen bonding along the peptide backbone. On the other hand, cluster 2 of $[\text{GA} + \text{K}]^+$ and $[\text{GA} + \text{Cs}]^+$ ions are also quite ordered ($\beta^4, ^4$ -helix) near the N-terminus, but the C-terminus appears to be disordered.

The influence of metal binding on neutral GA conformation was examined by comparing the secondary structure-forming tendencies of neutral and metal binding

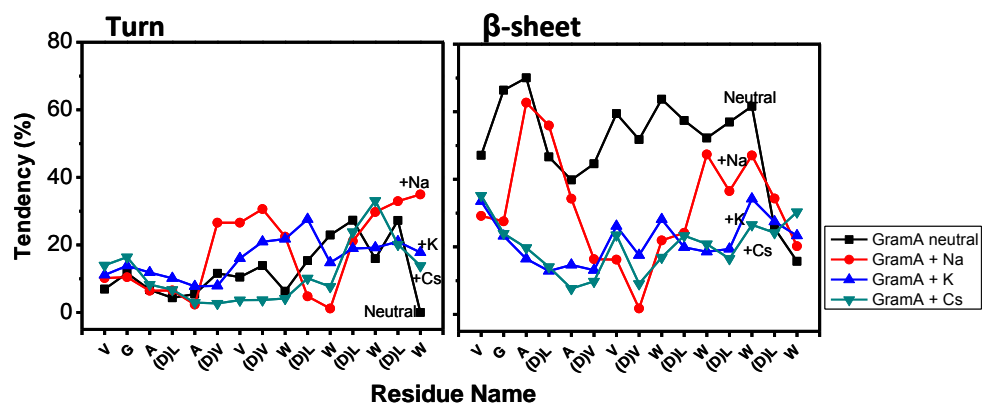


FIGURE 13. Turn and β -sheet-forming tendencies of neutral GA and $[\text{GA} + \text{met}]^+$ (met = Na, K, Cs) as a function of GA amino acid sequence.

forms. The backbone hydrogen bonds in all major clusters was examined using Kabsch and Sanders' DSSP program.¹¹⁵ Figure 13 contains plots of β -sheet and turn-forming tendency as a function of residue number. Turn-forming tendencies for neutral and metal ion bound forms range from 10-30%, whereas β -sheet-forming tendency are around 60% for neutral GA and decreases in the order $\text{GA} > [\text{GA} + \text{Na}]^+ > [\text{GA} + \text{K}]^+ \approx [\text{GA} + \text{Cs}]^+$ ions. The region DVal⁶-Val⁷-DVal⁸-Trp⁹ of $[\text{GA} + \text{Na}]^+$ ions significantly decrease in β -sheet-forming tendencies and increases in turn-forming tendencies to around 30%. $[\text{GA} + \text{K}]^+$ and $[\text{GA} + \text{Cs}]^+$ have very similar β -sheet-forming tendencies, around 20% across the entire sequence. The decrease in β -sheet-forming tendency is evidence that the disruption of intrinsic conformer preferences of GA may be related to the size of the alkali metal ion (see below).

Results from ITS-MDS reveal diverse gas-phase conformer preferences and CCS values for alkali metal ion adducts of GA (see Figure 11), and it is interesting to compare the fractional populations and CCSs of the various gas-phase conformers found by ITS-MDS with those obtained from electrospray ionization (ESI)-IMS measurement. Figure 14 contains arrival time distributions (ATDs) for $[\text{GA} + \text{met}]^+$ ions. There are several key points to note: (i) the ATDs for $[\text{GA} + \text{met}]^+$ ions are composed of multiple partially resolved profiles, (ii) the abundances of the two peaks for $[\text{GA} + \text{Na}]^+$ and $[\text{GA} + \text{Cs}]^+$ are approximately equal, whereas the ATD for $[\text{GA} + \text{K}]^+$ ions is dominated by a single component and (iii) the most abundant component of $[\text{GA} + \text{met}]^+$ are shifted to shorter time (smaller CCS) as the metal ionic radius increases. The peak centroids yield CCS of

406 Å² and 419 Å² for [GA + Na]⁺, 388 Å² and 405 Å² for [GA + K]⁺ ions and 391 Å² and 407 Å² for [GA + Cs]⁺ ions.

Calculated and experimental CCS profiles for [GA + met]⁺ (met = Na, K, or Cs) ions are over-layed in Figure 14A. For [GA + Na]⁺ and [GA + Cs]⁺ the fitted CCS profiles agree reasonably well with the experimental CCS profiles, which lends confidence to the structural assignment. The results for [GA + Na]⁺ and [GA + Cs]⁺ ions markedly contrast with that for [GA + K]⁺ ion, where the lower abundances of cluster 2 ($400\text{\AA}^2 \pm 6$, 9%) do not match the ITS-MDS predicted profile.

The reason(s) that the calculations under-estimate the population of cluster 2 of [GA + K]⁺ ions is not fully understood. These differences may be attributed to the experimental conditions as well as the parameters of monovalent ions in AMBER force field. Although empirical force fields are developed and validated by use of experimental and high-level *ab initio* computational data, it has been demonstrated that current AMBER adapted Åqvist's parameters¹¹⁶ may cause the formation of salt aggregates in the vicinity of biomolecular system, indicating the parameters of monovalent ions still need to be fine-tuned and thoroughly tested.^{117,118} On the other hand, these differences may also arise because ITS-MDS was carried out *in vacuo*, which may not accurately reflect the conformer preferences for ions formed by ESI. ITS-MDS is used to predict conformer preferences for gas-phase [GA + met]⁺, thus it is assumed that the gas-phase ions sample the entire free energy surface, which may not always be the case for ESI generated ions. That is, ions emerging from solution may not be able to evolve to preferred gas-phase conformers on the experimental time scale,

possibly owing to “freeze drying” of the ions by evaporative cooling during the ESI process.^{19,119} These issues are being examined further using both computational approaches and IMS experiments.

Experimental conditions could be another reason causing the discrepancy between experimental obtained and simulations predicted CCS profiles, for example ESI solvent effects, as observed for bradykinin $[M + 3H]^{3+}$ ions,^{22,27} suggest that solvent effects for $[GA + K]^+$ ion may differ from that for $[GA + Na]^+$ and $[GA + Cs]^+$ ions. It is also possible that conformer preferences for $[GA + K]^+$ are sensitive to collisional heating of the ions prior to ion mobility separation.^{22,27} These two potential effects were examined by comparing the experimental CCS profiles obtained using a number of electrospray solvent systems and by varying ESI source conditions that most strongly influence collisional heating prior to ion mobility separation.¹²⁰ These experiments clearly show that the CCS profiles are insensitive to ESI solvent and experimental conditions, which suggests that the ion conformers are not interconverting on the experimental time scale or the ion conformers are already re-thermalized in the trap region prior to injection into the ion mobility cell.

It is also possible that conformer preferences for $[GA + K]^+$ differ from those for $[GA + Na]^+$ and $[GA + Cs]^+$ ions. For example, as discussed above it appears that the β -sheet-forming tendency of $[GA + K]^+$ differs significantly from that for $[GA + Na]^+$. Polfer suggested that K^+ ions bound to dipeptides have a clear preference for a single binding configuration (C-terminal carbonyl oxygen) whereas Na^+ bound peptides involve multiple ligand types, *i.e.*, amide carbonyl oxygen atoms, cation- π interactions

and terminal NH_2 groups.^{121,122} Polfer described metal ion-peptide coordination in terms of the peptides wrapping around the metal cation, maximizing the electrostatic interactions with carbonyl oxygens,^{121,122} thus coordination could be influenced both by the size of the metal ion and the electron donor characteristics of the ligand. Another plausible explanation is that $[\text{GA} + \text{K}]^+$ ion conformers are highly fluxional owing to the weaker (relative to Na^+ ion) metal-ligand binding energy.¹¹²

The N-terminal formyl group is known to play an important role in the bioactivity of GA; however, the presence of this group inhibits some of the coordination chemistry described by Polfer et al.^{121,122} The influence of the formyl group on conformer preferences for binding metal ions was examined by comparing ATDs of $[\text{GA} + \text{met}]^+$ ions with that of $[\text{acetylated GA} + \text{met}]^+$ and $[\text{des-formyl GA (deGA)} + \text{met}]^+$ (see Figure 14B, 14C). The ATD for $[\text{acetylated GA} + \text{met}]^+$ (data not shown) is identical to that for $[\text{GA} + \text{met}]^+$, while the ATDs for $[\text{deGA} + \text{Na}]^+$ and $[\text{deGA} + \text{Cs}]^+$ appear slightly broadened, possibly indicating an increase in conformer diversity; however, the overall peak profiles are very similar to those for GA. Note also that the ATD for $[\text{deGA} + \text{K}]^+$ is very similar to that for $[\text{GA} + \text{K}]^+$ ions. It should be noted that the low abundance leading-edge peak (388 \AA^2) for $[\text{GA} + \text{K}]^+$ is less abundant for $[\text{deGA} + \text{K}]^+$ ions, and the CCS profiles for $[\text{deGA} + \text{Na}]^+$ ions exhibit trailing edge shoulder owing to a reduction in the abundance of the 419 \AA^2 CCS conformer(s). The similarities in ATDs between alkali metal adducts of GA and modified GA species suggest that under these experimental conditions the conformations of alkali metal adducts of GA, acetylated GA and des-formyl GA are similar.

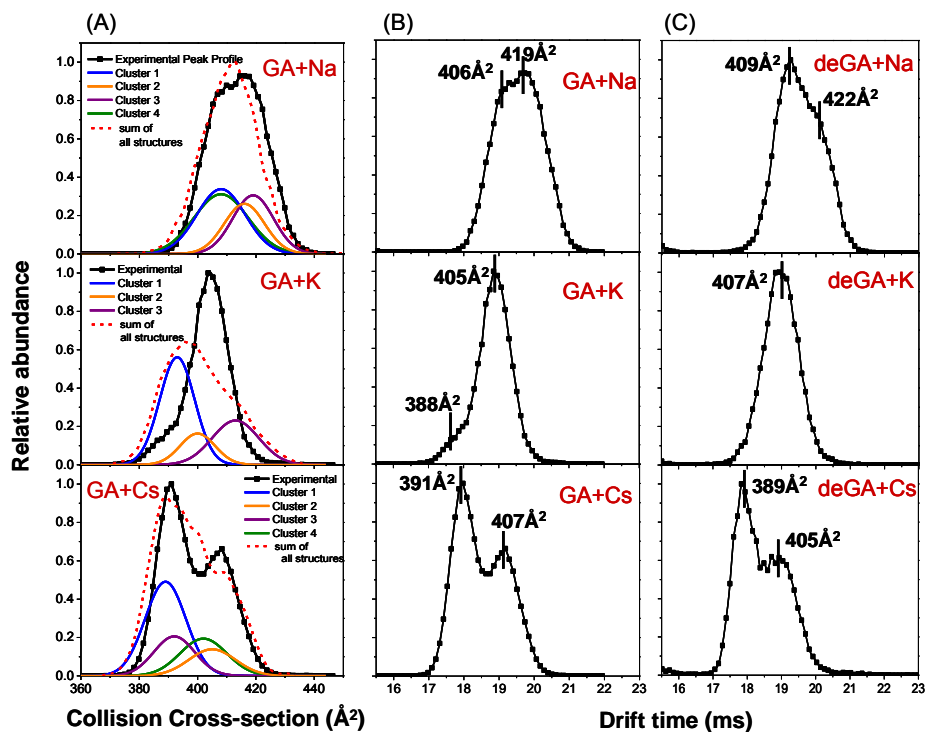


FIGURE 14. (A) Calculated collision cross-section (CCS) profiles by ITS-MDS for the most populated clusters for $[GA + \text{met}]^+$, $\text{met} = \text{Na}, \text{K}, \text{Cs}$. The red dashed line corresponds to the sums of each individual cluster. The experimental CCS profiles are shown in solid black lines. (B) Arrival time distributions of alkali metal (Na, K, Cs) adducts of gramicidin A. (C) Arrival time distributions of alkali metal (Na, K, Cs) adducts of des-formyl-gramicidin A. Centroid collision cross section values of major peaks are labeled in the figure.

Conclusions

The interaction of metal ions with peptides has been investigated by using various gas phase techniques and theoretical calculations.¹²¹⁻¹²⁴ Here, we present a systematic study of how alkali metal ion (Na^+ , K^+ , Cs^+) influences conformations of low internal energy gas-phase peptide ions by using ITS-MDS and ion mobility spectrometry (IMS). First, ITS-MDS was performed on the neutral GA *in vacuo* to investigate the intrinsic conformer preferences of GA, and the simulations strongly suggest a high β -sheet-forming tendency throughout the entire sequence as also suggested by previous studies.⁹⁷ In spite of the large conformational differences between these structures, the predicted abundance (free energy) of each conformation is quite similar, implying considerable intrinsic structural flexibility of GA *in vacuo*, which is also a good indication of its structural flexibility in condensed phase. Comparing the neutral GA and $[\text{GA} + \text{Na}]^+$, the degree of structural similarity is significantly high for these two species.

The calculated CCS of the most abundance conformers found by ITS-MDS for metalated GA decreases in the order $[\text{GA} + \text{Na}]^+ (408 \text{ \AA}^2) > [\text{GA} + \text{K}]^+ (393 \text{ \AA}^2) > [\text{GA} + \text{Cs}]^+ (389 \text{ \AA}^2)$ as shown in Figure 11. This order agrees very well with the experimental CCS for the most abundant peaks in Figure 14. In addition, the calculated CCS profiles of $[\text{GA} + \text{Na}]^+$ and $[\text{GA} + \text{Cs}]^+$ ions determined from ITS-MDS agree reasonably well with the experimental values. The agreement between the measured and calculated CCS provides high confidence of the structural assignment. On the other hand, there are noticeable differences in the ITS-MDS predicted and measured CCS

profile of $[GA + K]^+$ ions. ITS-MDS predicts three conformers (393 \AA^2 , 400 \AA^2 and 413 \AA^2), all of which are observed experimentally; however, the predicted and measured abundance are significantly different; further investigation is under way to delineate the reasons for the differences.

Secondary structure-forming tendencies were calculated for neutral GA and $[GA + \text{met}]^+$. High β -sheet-forming tendency for neutral GA further confirms the intrinsic propensity of GA sequence to form β -helix type of structure. In addition, upon metal ion adduction, β -sheet-forming tendency decreases in the order $GA > [GA + Na]^+ > [GA + K^+] \approx [GA + Cs]^+$ ions.

Alkali metal ions are known to interact strongly with the π -electron system of aromatic side chain groups as observed for amino acids and small peptides.^{121,122} Although GA contains four Trp residues, the alkali metal ion favors coordination by the amide carbonyl oxygen atoms. Evidence for cation- π interaction was only found for conformer 2 of $[GA + Na]^+$ ion where Na^+ ion appears to be coordinated by the Trp¹⁵ side chain. The conformation of $[GA + \text{met}]^+$ depends on the competition between backbone amide carbonyl oxygen atoms and Trp side chain, but for K^+ and Cs^+ metal ion coordination strongly favors amide carbonyl oxygen atoms. This result could be due to the fact that parameters of monovalent ions in the AMBER force field only approximately takes into account the charge- π interaction through the cation/aromatic carbon van der Waals interactions and errors could exist.

CHAPTER V

SOLUTION-PHASE CONFORMATIONS AND CONFORMATIONAL TRANSITION

KINETICS OF GRAMICIDIN A

Introduction

Peptide/protein self-assembly and aggregation represent important biological activities that include essential cell functions from ion channels to cell destruction/lysis^{125,126} and even disease, *i.e.*, protein misfolding diseases such as Alzheimer's, Parkinson's, Mad Cow and type II diabetes.¹²⁷ The activity of membrane-associated peptides *in vitro* and *in vivo* depends on their propensity to bind to membranes and self-assemble to bioactive states.¹²⁸ Although intensive efforts are focused on characterizing lipid-peptide¹²⁹⁻¹³¹ and peptide-peptide interactions^{132,133} and understanding how such interactions are influenced by the conformation of the monomeric subunits,^{19,35,134} understanding how folding dynamics and electrostatic interactions, such as intermolecular hydrogen bonding, affect self-assembly of peptides in low dielectric environment, *i.e.* lipid vesicles,¹³⁵ lipid bilayers,^{129,136-138} and as native complexes;^{18,139} remains as a major challenge to structural biology. Equally challenging is the need to directly monitor the kinetics of self-assembly/disassembly processes under native conditions. Such studies will potentially provide molecular-level understanding of self assembly mechanism of a range of bioactive peptides, *i.e.*, gramicidins, protegrins and cecropins, which possess a broad spectrum of bioactivity, ranging from antibacterials and antiinflammatories to potential treatment of cancer and tumors.

The family of gramicidin peptides are unique because of their small size and specificity of biological function, i.e., monovalent ion channels.¹⁴⁰ Gramicidin A (GA), a linear pentadecapeptide isolated from soil bacterium *Bacillus brevis*, has been extensively investigated using a variety of experimental and computational tools; however, numerous questions concerning the conformer preferences and the environment-dependent conformer preferences remain unanswered. GA forms single-stranded, right-handed $\beta^{6,3}$ -helices with inter-molecular hydrogen bonds between their N-termini. Such head-to-head helical dimers are also known to exist in artificial lipid bilayers and micelles as demonstrated by solution-phase nuclear magnetic resonance (NMR).¹⁴¹ In solution, GA exists in a monomer-dimer equilibrium as well as an equilibrium between different dimer conformations, and the distribution of these species depends on solvent polarity, concentration, and temperature.¹⁴² For example, in polar solvents, i.e., TFE or H₂O, GA exist predominantly as a monomer, whereas in alcohols significant amounts of dimer are present.⁹⁴ More interestingly, the self-assembled behavior of GA is known to be highly sensitive to the environment.^{94,99,100,142-144} The environment-dependent conformations of dimeric GA have been examined in details by various techniques, including CD,^{94,99,142,144,145} NMR,^{141,146-148} liquid chromatography,^{95,149-151} X-ray crystallography,^{102,106,147,152,153} and mass spectrometry.^{96,154,155}

Although techniques such as CD, Raman or NMR provide evidence for the detailed structural elements, interpretation of the data is often ambiguous owing to an equilibrium distribution of conformations as both monomer and dimer species, which

complicates monitoring variations in the abundances of the different species and the determination of kinetics of self-assembly. Ion mobility spectrometry (IMS), an ion size-based separation technique provides a unique means for simultaneous and direct analysis of diverse conformer populations in the mixture, which are used to monitor microheterogeneity of the ion population.¹⁹ Furthermore, different conformations that comprise the ion population are also distinguished by using hydrogen/deuterium exchange (HDX).⁷³ Although HDX is a powerful tool for studying peptide and protein folding/unfolding dynamics, combining HDX and IMS has added benefit for exploring the conformational space of biomolecules.⁷⁴ Lastly, the experimental data are compared with candidate conformations derived from molecular dynamics simulations.

The GA dimer has been previously studied by MS-based techniques.^{96,154,155} Dobson *et al.* used ESI-MS to probe solvent effects on the formation of GA,¹⁵⁴ and HDX ESI-MS data reveals an extremely slow exchange process indicating a highly structured configuration of GA dimer.^{96,154} On the other hand, detail kinetic measurements for monomerization reactions of GA dimer as well as the conformation(s) or interconversion of GA dimer have not yet explored by MS-based techniques. Here, we present a comprehensive study combining native electrospray ionization (ESI),^{15,119,156} ion mobility-mass spectrometry (IM-MS), molecular dynamics simulations (MDS) and HDX to characterize the monomerization and dimer conformer preferences that provide new insights to the solution-phase self-assembled behavior of GA.

Experimental Methods

Gramicidin (*Bacillus brevis*) purchased from Fluka Chemicals (Sigma-Aldrich) is a natural mixture containing approximately 80% gramicidin A and small amounts of gramicidin B and C, and this sample was used without further purification. The concentration of 1 μ M of gramicidin (mixture of gramicidin A, B and C) were used for monitoring the monomerization process using ESI-IM-MS. High-purity ($\geq 90\%$) gramicidin A purchased from Sigma-Aldrich (St. Louis, MO) was used for the HDX experiment. Ethanol, n-propanol, isobutanol, and methanol-OD were also purchased from Sigma-Aldrich (St. Louis, MO).

The ESI-IM-MS spectra from various solvents were acquired on a Waters SynaptTM HDMS G2 mass spectrometer (Waters UK Ltd., Manchester, UK) equipped with a travelling-wave ion mobility cell maintained at 3 mbar of nitrogen. Ions were formed by nano-ESI using a source temperature of ~ 100 °C and capillary voltage 1.6-2.2 kV. The cone and extraction voltages are set to produce the high abundance of the dimer signals. For the IM experiments, the traveling wave ion mobility cell was operated at wave velocity of 550 m/s and wave amplitude of 38 V.

The percent of monomer from the ESI-IM-MS experiments was represented by the ratio of ion abundances calculated using the areas of the ion mobility arrival time distribution (ATD) for the dimer divided by the sum of the monomer and dimer abundances. The ATD of GA dimer profile can be deconvoluted into three individual Gaussian distributions. The percent of different conformers of the dimer was then obtained by computing the ratio of the abundances of the conformer to that of the sum

intensity of the monomer and dimer. Assuming the solid material is initially dimer and at low concentration as in the ESI experiment, the monomerization process follows a simple first order exponential decay.¹⁴²

To determine the collision cross section (CCS) of the dimer conformers from IM drift time measurements, the CCS calibration were performed according to the protocol described previously by Ruotolo et al.⁵⁴ The calibration standards included tryptic peptides obtained from cytochrome c and myoglobin. Literature values of CCS of the calibrant peptides were taken from the database generated by Clemmer and coworkers.⁵⁵

Fully deuterium-labeled gramicidin A samples were prepared by incubating the gramicidin A in methanol-OD at a concentration of 1 mM for over 24 hours. The stock solution was then diluted to 1 μ M in n-propanol to initiate the back-exchange. The time between mixing the solution and initiating the MS measurement is about 2 min. Mass spectra were taken over time to monitor the back-exchange. Changes in deuterium content (in Da) were calculated by comparing the average mass-to-charge values of the isotope clusters of the partially deuterated peptides with that of non-deuterated peptides.

Three PDB bank dimer structures were selected as starting structures for the MD calculations (1MIC, 1ALZ, and 1JNO). These conformers represent the three most commonly observed conformers of the dimer; parallel double helix (1MIC), antiparallel double helix ion-free (1ALZ), and head-to-head dimer (1JNO). The simulations were initiated with a specific starting structure (1MIC, 1ALZ, or 1JNO) and placing two Na⁺ ions at random positions around the molecule; the simulations were repeated using 7 different initial starting positions of the Na⁺ ions. MDS were run at 300 K on each PDB

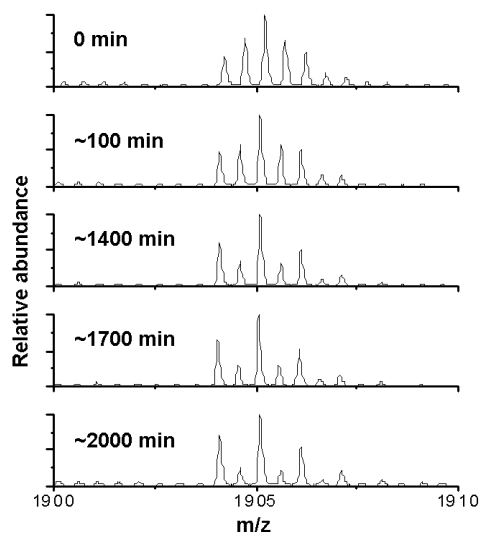
dimer structure with/without two Na^+ present *in vacuo* for 50 ns using AMBER 9.0, after which each structure was energy-minimized. AMBER FF99SB force field was used. Trajectory method cross section calculations were carried out every 10 ps for each structure. In all trajectories, the starting PDB structures eventually converged to give one or more steady-state structures with little change in backbone Ca -rmsd and collision cross section values. The average cross section of last 5 ns (500 structures) for each trajectory was used for comparison with the experimental values.

Results and Discussion

Gramicidin A (GA) is a naturally occurring linear pentadecapeptide isolated from soil bacterium *Bacillus brevis*. The sequence of GA is HCO-Val-Gly-Ala-DLeu-Ala-DVal-Val-DVal-Trp-DLeu-Trp-DLeu-Trp-DLeu-Trp-NHCH₂CH₂OH. Due to its highly hydrophobic nature, when ionized by ESI the dominant ions observed correspond to Na^+ ion containing species. The Na^+ ions are present in the solvents and the peptide sample, and no attempts were made to remove these ions. These studies are also limited to peptide species with Na^+ ions, and comparable data for other monovalent ions (K^+ , Cs^+ , or Rb^+) were not investigated because addition of these salts changes the equilibrium species owing to changes in the solution ionic strength.

The ESI mass spectrum of gramicidin A contains abundant ion signals between m/z 1905-1909 that correspond to $[\text{GA} + \text{Na}]^+$ and $[2\text{GA} + 2\text{Na}]^{2+}$ ions (see Figure 15A). These ions have the same m/z ratio, but the isotope cluster for ions that carry a single charge are separated by one mass unit, whereas the ions that carry two charges are

(A)



(B)

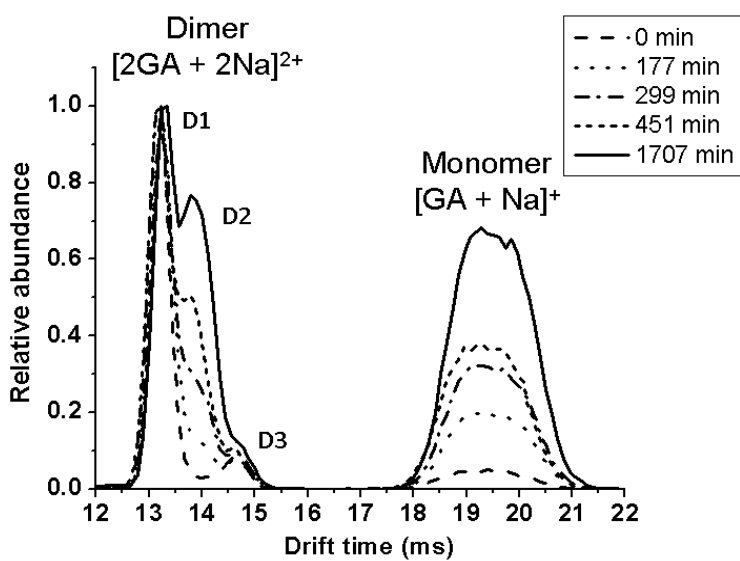


FIGURE 15. (A) Zoom-in mass spectra of GA incubated in n-propanol as a function of time showing the m/z 1905 region of $[GA + Na]^+/[2GA + 2Na]^{2+}$. (B) Ion mobility arrival time distributions of mass envelope of m/z 1905.

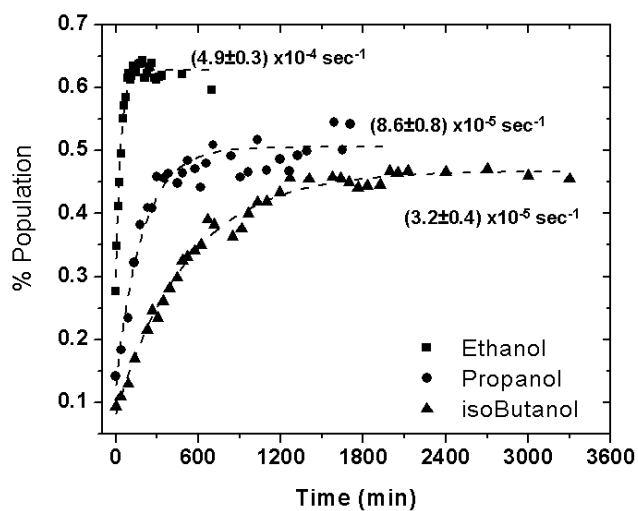


FIGURE 16. The kinetic profiles of the monomerization of GA at a concentration of 5 μM for a series of ethanol, propanol and isobutanol, expressed as the intensity ratio of monomers as a function of incubation time. The rate constants are indicated on the plot.

separated by 0.5 mass units. The ion abundance ratio of $[GA + Na]^+/[2GA + 2Na]^{2+}$ increases as a function of time owing to disassociation of GA dimer in the alcohol solution (see Figure 15A), thus it appears that in the lyophilized powder GA exist as a dimer that slowly dissociates to monomer in alcoholic solution. The signals for $[GA + Na]^+$ and $[2GA + 2Na]^{2+}$ can be clearly distinguished on the basis of ion mobility (Figure 15B), and the abundances of the corresponding ions changes as a function of incubation time.

The kinetics of the monomerization reaction was determined by using the abundances of ion mobility separated monomer (see Figure 15B). Figure 16 contains plots of the abundances ratio of monomer and dimer ions as a function of incubation time. It is apparent that in all cases the equilibrium favors monomer at longer incubation times; however, the rate of monomerization and the relative abundances of monomer and dimer species at equilibrium are solvent dependent. That is, the kinetics of monomerization is slower for the longer chain alcohols and the abundance of the dimer also increases with increasing chain length. The measured rate constants $(4.9 \pm 0.3) \times 10^{-4}$, $(8.6 \pm 0.8) \times 10^{-5}$, and $(3.2 \pm 0.4) \times 10^{-5} \text{ sec}^{-1}$ for ethanol, propanol and isobutanol, agree very well with the literature values $(5.0 \pm 0.4) \times 10^{-4}$, $(8.2 \pm 0.7) \times 10^{-5}$, and $(2.5 \pm 0.4) \times 10^{-5} \text{ sec}^{-1}$ obtained by HPLC and fluorescence measurement.¹⁵⁰

The ion mobility arrival-time distribution (ATD) for the dimer ions is composed of three distinct (overlapping) Gaussian distributions, labeled D1, D2, and D3, and the abundances of each species is time dependent (Figure 15B). Note that the D2 becomes more abundant over time with respect to D1 and D3, despite the overall decrease in

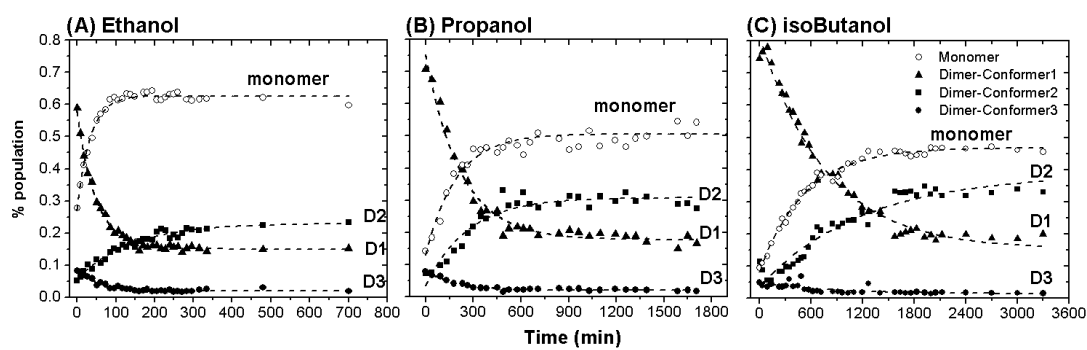
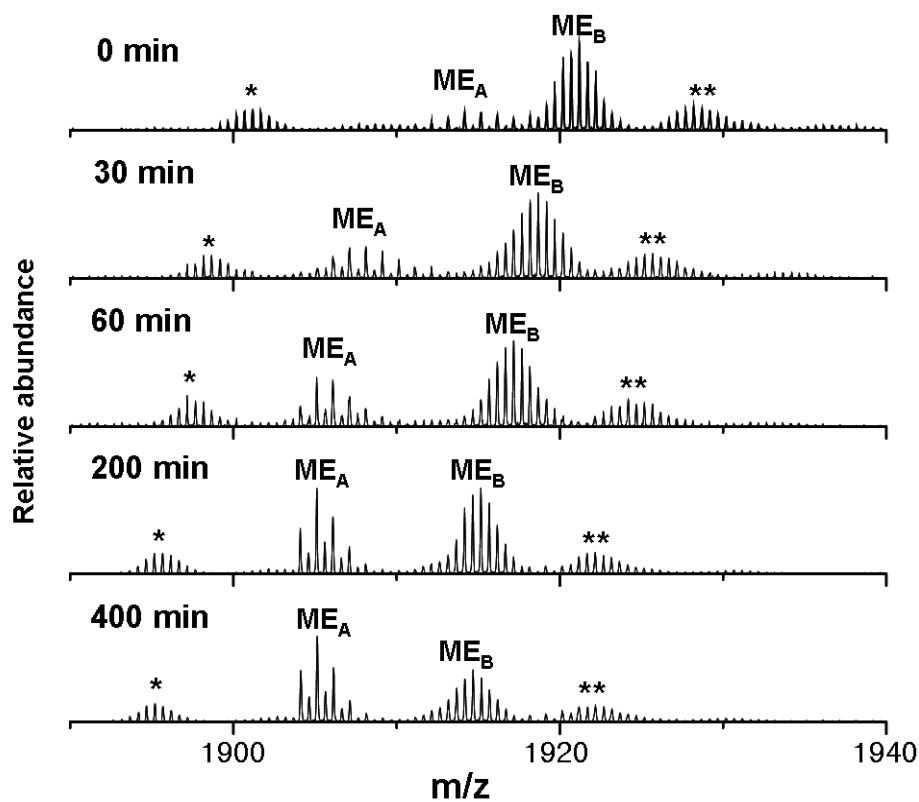


FIGURE 17. The kinetic profiles of three dimer conformers (D1, D2, D3) in ethanol (A), propanol (B), and isobutanol (C). The monomerization kinetic profile is also shown in comparison (open circle).

relative abundance of dimeric species. To quantify the kinetics of the dimer disassociation, the relative abundances of D1, D2 and D3 were estimated from the abundances of each conformer peak divided by the sum of the abundances of the total area of the dimer profile. The resulting kinetic profiles for D1, D2 and D3 in different solvents are shown in Figure 17; note that in each solvent the abundance of D1 and D2 greatly exceeds that of D3, which is only about 5 % in all three alcohols. Relative abundances of D1, D2 and D3 at equilibrium in alcohol solution are solvent dependent and summarized in Table 1. While the population of D3 stays less than 5%, D2 becomes more abundant and D1 becomes less abundant as the alcohol chain length increases.

Solution-phase HDX was performed as a means to investigate differences in conformers D1, D2 and D3. Figure 18 contains a portion of the mass spectrum of GA, specifically the m/z region corresponding to the isotopic envelopes for deuterated $[GA + Na]^+$ and $[2GA + 2Na]^{2+}$ ions. Two distinct mass envelopes (ME_A and ME_B) are labeled in the figure; ME_A is composed of a mixture of single-charged monomer ions (separated by 1 amu) and double-charged dimer ions (separated by 0.5 amu), while ME_B consist entirely of double-charged dimer ions. Both mass envelopes are shifted to lower m/z values with increasing incubation time; however, the shifts occur at different rates, which suggest the rates of HDX for ME_A and ME_B are quite different. Such bimodal isotope patterns are consistent with an EX1 mechanism as noted previously by Gross et al. for HDX of GA in n-propanol.⁹⁶



* signal for GA $[GA + H]^+$ ions

** signal from impurities

FIGURE 18. H/D back-exchange mass spectra of GA in n-propanol as a function of time. The mass spectra contain two distinct mass envelopes of GA labeled as Mass Envelope A (ME_A) and Mass Envelope B (ME_B).

Figure 19 contains the plot showing the time-dependent change in deuterium content for ME_A and ME_B. They are fitted by a series of first-order rate expressions according to the expression below:^{157,158}

$$\ln(D) = -k_{\text{ex}}t + \ln(H_{\text{tot}}) \quad (7)$$

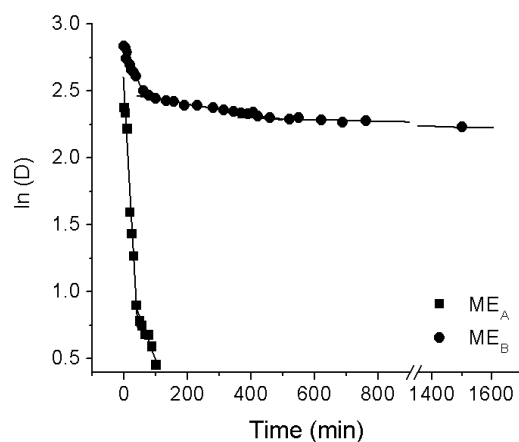
where D is the number of protected deuteriums, H_{tot} is the total number of exchangeable hydrogens, k_{ex} is the HDX rate constant, and t is the incubation time. Different groups of hydrogens with different exchange rates can be easily distinguished from the natural logarithm plot. For example, three populations of exchangeable hydrogens are present in ME_A and four populations of exchangeable hydrogens are present in ME_B. A summary of different hydrogen groups and the corresponding exchange rates are listed in the table in Figure 19. The fast-exchange group represents hydrogens that have exchanged within the time between mixing the solutions and initiating the MS measurements, which is about 2 min; hence the exchange rate of this group cannot be accurately determined. There are 11~12 fast-exchange hydrogens for ME_A and 5~6 for ME_B. The intermediate exchange rates comprise 9~10 hydrogens for ME_A and 7~8 hydrogens for ME_B. The exchange rate of intermediate groups for ME_A is significantly faster than that of ME_B; estimated to be about 10 fold faster for group intermediate 1 and 100 folds faster for group intermediate 2. For ME_A, all exchangeable hydrogens are exchanged in less than 150 min. Conversely, the slow-exchange of ME_B starts from ~500 min, and there are 7-8 hydrogens that do not undergo exchange at times greater than 1600 min.

The positions of the 7~8 deuteriums retained by ME_B after 1600 min were probed by using collision-induced dissociation (CID) on the ME_B mass envelope. The extent of

scrambling is known to be dependent on the charge carrier being proton or an alkali metal ion, that is, fragmentation of the sodium-cationized species resulted in much less scrambling when compared to the protonated species.¹⁵⁹ Figure 20 contains the CID product ion spectrum of the $[GA + Na + 8]^+$ ion shows mostly N-terminal (a_n) and C-terminal (y_n) fragment ions many of which retain the labeling information. The numbers of deuterium in the fragment ions were determined from differences in the centroids of the mass envelopes between ME_B and the fragment ions of the non-deuteriated of $[2GA + 2Na]^{2+}$ ions. The CID spectrum of the ME_B ions suggests that the non-exchanging hydrogen lies mostly between residue DVal⁸ and residue DLeu¹².

HDX clearly suggest two distinct dimer populations (ME_A and ME_B), and further evidence for this is indicated by the ion mobility data for the partially deuterated species (see Figure 18). That is, ATDs for ME_A and ME_B reveal very different features: the ATD of ME_A clearly indicates a higher abundance of D1, ~54% of conformer D1 as compared to 37% for the total population at equilibrium (see Figure 16). Conversely, the ATD for ME_B contains higher abundance of D2, ~68% of conformer D2 as compared to 59% of D2 for the entire population at equilibrium. Finally, D3 is only observed under the fast exchange ME_A ATD profile.

The protein data bank contains three distinct conformers for GA dimers: (i) parallel double helix (1MIC), (ii) antiparallel double helix (1ALZ), and (iii) head-to-head dimer (1JNO). MDS was used to generate representative structures of $[2GA + 2Na]^{2+}$ using each PDB structure. The $[2GA + 2Na]^{2+}$ conformers were generated by placing the two Na^+ ions at random positions on the starting conformers. For all



| Hydrogen Group | ME _A | | ME _B | |
|----------------|--------------------------|------------------|--------------------------|------------------|
| | Rate / sec ⁻¹ | No. of hydrogens | Rate / sec ⁻¹ | No. of hydrogens |
| Fast | Not determined | 11.5 | Not determined | 5.4 |
| Intermediate1 | 6.7X10 ⁻⁴ | 8.6 | 9.1X10 ⁻⁵ | 5.4 |
| Intermediate2 | 1.1X10 ⁻⁴ | 0.9 | 6.6X10 ⁻⁶ | 1.8 |
| Slow | | | 1.0X10 ⁻⁶ | 0.8 |

FIGURE 19. Time-dependent change in deuterium content of GA monomer log scale. The maximum number of exchangeable hydrogens is 21 for GA monomer. Hydrogen groups are separated based on similar exchange rate. The numbers of hydrogens and rate constant for each hydrogen groups are shown in the table.

trajectories, the starting structures eventually converged to one steady structure with little change in backbone C α -rmsd values. Collision cross-sections were calculated over the course of the simulations. The average CCS was calculated using last 5 ns simulations. Figure 22A compares the calculated CCS from all trajectories with experimental obtained GA dimer CCS profiles. Figure 22B contains selected candidate structures that contain Na⁺ ions, which match the CCS for each conformer (D1, D2, and D3). Independent of the starting position of Na⁺ ions, Na⁺ migrates to the interior of the helix with few exceptions in which one Na⁺ ion is surrounded by a couple of TRP side chains. In most cases, Na⁺ ions form electrostatic interactions with backbone carbonyl oxygens, which in turn would disrupt or weaken the nearby inter-molecular hydrogen bonds. In addition, with Na⁺ ions at different starting positions, the equilibrated structures in the end of the simulations are different from each other, hence with different CCS. In summary, CCS for candidate structures generated from 1MIC are within the range of experimental CCS for D1 and D2, *i.e.*, two of the calculated conformers fall within the range of D1 and four are within the range of D2, but none are in the range of D3. Candidate conformers for 1ALZ are fall within the range of D2, whereas the CCS for 1JNO has CCS fall within the range for D3 conformers.

This study yields new insights regarding the time- and solvent-dependence for the monomer-dimer equilibrium (Figure 15 and Figure 16) and the transitions between different dimer conformations of GA (Figure 17). The decrease in the monomer abundance at equilibrium as the hydrocarbon chain length increases suggests that the stability of the dimer is significantly influenced by the ability of the solvent to compete

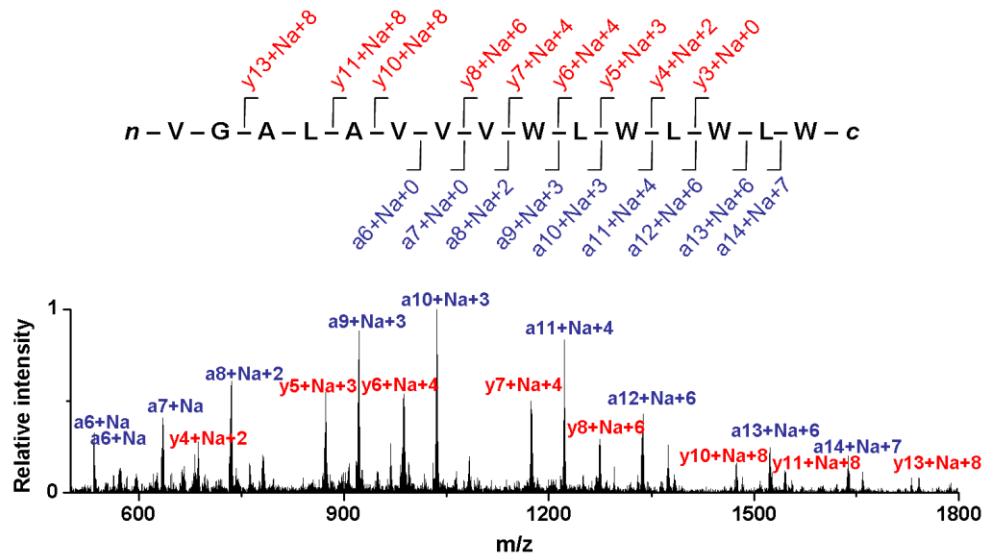


FIGURE 20. CID product ion spectrum of the $[GA + Na + 8]^+$ ion. Mass shift from $[GA + Na]^+$ is labeled for a- and y-type fragment ions.

for the intermolecular hydrogen bonds that stabilize the dimer. In addition, changes in ATD (Figure 15B) as a function of incubation time reflect the kinetics of the monomerization reactions as well as changes in the abundances of dimer conformers, *i.e.*, D1, D2 and D3. For example, the equilibrium abundance of D1 decreases and that of D2 increases as a function of incubation time (Figure 17) and solvent polarity (Table 2). Finally, the kinetic rates of the monomerization reaction (see Figure 16) for the different alcoholic solutions agree very well with those previously reported,¹⁵⁰ thus this study provides further data that supports the view that ESI-MS data accurately reflects the distribution of species in solution.^{19,22,160}

The GA monomer-dimer equilibrium is influenced by the solvent polarity,^{96,155} and IM-MS measurements show that the solvent polarity has a strong influence on the distribution of conformers D1 and D2 (see Table 2), *e.g.*, D2 is clearly favored over D1 in the less polar solvents. Previous studies on conformer preferences of GA dimer suggest that in alcoholic solutions GA monomers assemble to form both parallel and anti-parallel β -helix dimers.⁹⁴ For example, Wallace reported equilibrium abundance for the antiparallel β -helix dimer of 57 %, 64 % and 65 % in ethanol, propanol, and butanol, respectively;⁹⁹ these values are in excellent agreement with the IM-MS measured values for D2: 54 %, 59 % and 61 % in ethanol, propanol, and isobutanol (see Table 2). That is, the anti-parallel double β -helix dimer is favored in less polar solvents,^{5,144} further evidence that D1 is most likely the parallel double β -helix and D2 is the antiparallel double β -helix dimer.

TABLE 2. Relative abundances of three conformers (D1, D2, and D3) of GA dimer in ethanol, propanol and isobutanol at equilibrium.

| Solvent | Dimer -D1 (%) | Dimer-D2 (%) | Dimer-D3 (%) |
|------------|---------------|--------------|--------------|
| Ethanol | 41 | 54 | 5 |
| Propanol | 37 | 59 | 4 |
| isoButanol | 36 | 61 | 3 |

The assignment of specific conformations for D1 and D2 were evaluated further by using molecular dynamics simulations. Calculated CCS for the three PDB structures (1MIC, 1ALZ and 1JNO) compare favorably with the experimental CCS profile (see Figure 22A). The calculated CCS for parallel double helix (1MIC) fall within the range of the experimental CCS for both D1 and D2; while the calculated and experimental CCS for anti-parallel double 1ALZ fall entirely within the range for D2. Candidate structures generated by using head-to-head dimer (1JNO) as the starting conformer are scattered across the entire range for D1, D2 and D3. However, the only calculated CCS in the range of D3 is from 1JNO. Comparison of the CCS data suggests that D1 and D2 are most likely the parallel and anti-parallel double β -helix, respectively, whereas D3 corresponds to a head-to-head dimer composed of monomer $[\text{GA} + \text{Na}]^+$ ions. CCS and candidate conformations for $[\text{GA} + \text{Na}]^+$ monomer ions were reported previously,²³ and the experimental CCS for D3 appear to be consistent with a dimer of these ion forms, e.g., possibly a non-specific ionic complex formed during the ionization process.

The solution-phase HDX experiments provide more detailed information regarding the GA dimer conformer preferences. The back-exchange reaction of the GA dimer in n-propanol reveals the presence of two distinct conformer populations, *i.e.*, the population of ions corresponding to ME_B undergoes HDX extremely slow suggesting the presence of well-protected hydrogen-bonding network, and the much faster rate of HDX for ME_A corresponds to conformations that are more solvent accessible. Furthermore, the distinct separation in the two m/z envelopes (ME_A and ME_B) suggests that these conformer populations are not inter-converting prior to monomerization.

HDX rates and numbers of exchanges vary depending on their local environment, *i.e.*, solvent accessibility, electrostatic charge and participation in H-bonding.¹⁶¹ It is instructive to consider the complete inventory of exchangeable hydrogens in both GA monomer and dimer ions. GA monomer ions contain 21 exchangeable hydrogens, 15 backbone amide hydrogens, 4 hydrogens on the TRP side-chain, 2 hydrogens on the C-terminal ethanolamine group and 1 hydrogen on the N-terminus. The β -helix dimers (both parallel and anti-parallel) contain 28 labile backbone hydrogens that are involved in intermolecular hydrogen bonds (14 per monomer), which protected against exchange. Based on the extreme slow rate of exchange, ME_B most likely corresponds to conformers with protected hydrogen-bonding network, either parallel or antiparallel, while the conformers for ME_A, which fully exchanged with 150 min, represent disorder structures that are more solvent accessibility.

The mass envelop ME_B rapidly exchanges 5-6 hydrogens between initiating the back-exchange and recording the first mass spectrum) (Figure 19), and these are assigned to the 4 indole hydrogens and the terminal groups. 7~8 hydrogens exchange with intermediate rates (within 500min) and the remaining hydrogens undergo slow-exchange (500min to 1600min), which are most likely backbone amide hydrogens. The most protected deuterium for ME_B (7~8 that have not exchanged after 1600 min) appear to be located between residues 8 and 12, this assignment is confirmed by CID spectrum of the ME_B ions (Figure 20). Note also that this assignment agrees with solid-state NMR results on HDX behavior of GA with ordered structures in hydrated lipid bilayers

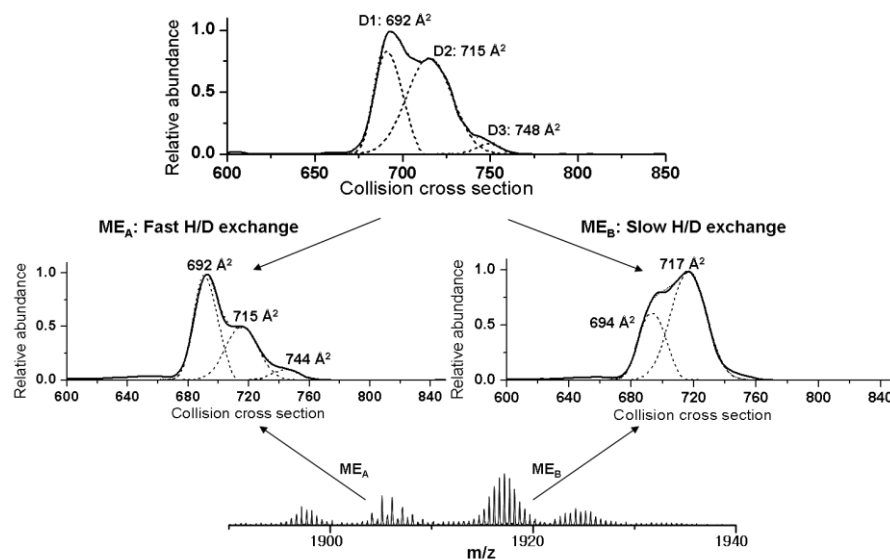
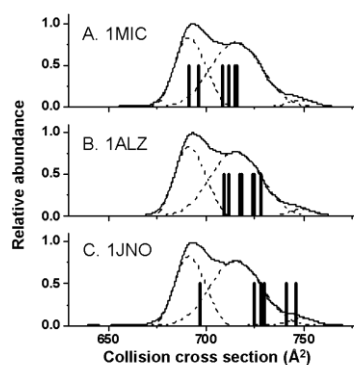


FIGURE 21. Collision cross section profiles of Mass Envelope A (ME_A) and Mass Envelope B (ME_B) of GA undergoing H/D back-exchange in n-propanol. Only the GA dimer profiles are shown. The GA dimer profile without HDX is also shown in comparison.

reported by Cross *et al.*; they identified 8 hydrogens that were non-exchangeable and located in the middle of the backbone region.¹⁴⁸

HDX combined with ion mobility provides a means to distinguish the sub-populations of D1 and D2 (see Figure 21). The ATDs for ME_A and ME_B contain signals for both D1 and D2, but the relative abundances of the two conformers are quite different, which suggests that ordered and disordered hydrogen-bond networks may be present in D1 and D2. This may be a result of the coordination of the Na⁺ ions by the backbone amide groups, *i.e.*, Na⁺ may disrupt the hydrogen-bonding network that stabilizes the double helix dimer. Note that the two conformers shown in Figure 22B for the parallel double helix (1MIC), which differ in terms of Na⁺ ion binding sites, appear to be more disordered near the N-terminus when both Na⁺ ions are located near the C-terminus. These disordered regions are expected to increase the rate of HDX. On the other hand, the anti-parallel double helix (1ALZ) appears to maintain a higher degree of order regardless of the positions of the two Na⁺ ions. Note that the exterior of 1ALZ is less solvent accessible owing to increased hydrophobicity as a result of having bulky tryptophan residues located at both ends of the dimer. That is, for 1ALZ the only polar solvent accessible sites of the dimer are at the very ends of the channel, whereas the solvent accessible sites for 1MIC extend from the N-terminus of the complex to approximately the middle of each chain. This situation is analogous to TRPZIP4 where the bulky tryptophan residues forms a more compact hydrophobic core that protect the native hydrogen bonds that stabilize the β -hairpin.¹⁶² Note also, that a similar argument can be used to rationalize a smaller CCS for D1 relative to that of D2. For example, the

A.



B.

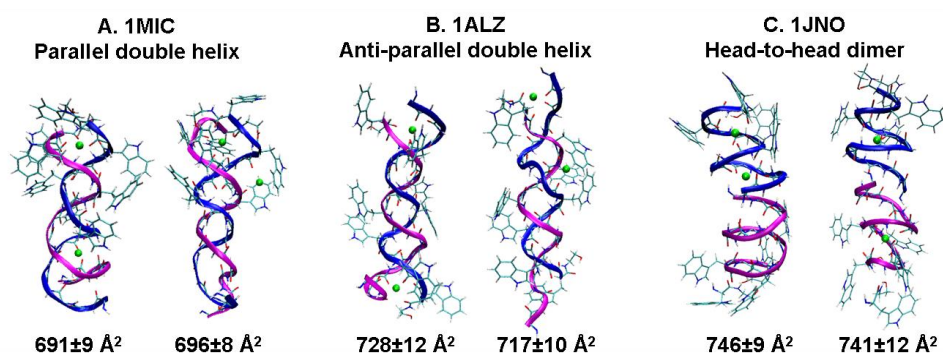


FIGURE 22. The comparison of calculated collision cross-sections of GA dimer candidate structures generated from PDB structures 1MIC (A), 1ALZ (B), and 1JNO (C) with experimental obtained CCS profiles. Selective candidate structures generated from three PDB bank structures: 1MIC (A), 1ALZ (B) and 1JNO (C). Calculated collision cross sections for each structure are labeled in the figure. The backbone is shown in ribbon representations. Two monomer chains are color-coded in blue and magenta. All TRP side-chains are shown in cylinder representation. Na^+ ions are indicated in green color.

disordered terminus of D1 decreases the length of the double helix, thus allowing for compaction of the strands comprising the double helix, whereas the more ordered termini of D2 are less dynamic and the double helix conformation is retained.

Conclusions

The ESI-IM-MS clearly shows that the equilibrium abundances of GA dimer conformers are dependent on solvent polarity. For example, distinct dimer conformers (denoted here as D1, D2 and D3) are detected and the equilibrium abundances of these species vary with solvent polarity. It appears that the least abundant of the dimer ions, viz. D3, is best described as a non-specific complex that is formed during the ESI process. Although weakly bound, non-specific complexes are observed in ESI mass spectra, these complexes do not accurately reflect condensed phase functional complexes. On the other hand, the strong correlation between the solution phase and ESI-MS determined kinetics of monomerization provide compelling evidence that the GA dimer populations reported herein represent real solution-phase GA dimer conformers; this conclusion is further supported by the excellent agreement between ESI-MS and previously reported NMR HDX for the native hydrogen-bonding network. Furthermore, calculated CCS for candidate structures generated by molecular dynamics are in excellent agreement with the CCS measurement.

Molecular dynamics simulations and HDX experimental data are interpreted as evidence that D1 and D2 corresponds to parallel and anti-parallel dimers, respectively. These assignments are consistent with previous reported values in different solvents.¹⁵⁰

In addition, no evidence is found to suggest that D1 and D2 interconvert in route to monomerization.

Molecular dynamics simulations were used to evaluate candidate conformations of $[2GA + 2Na]^{2+}$ ions of three PDB structures (1MIC, 1ALZ, 1JNO) of the GA dimer. CCS D2 (antiparallel double helix) and D1 (head-to-head dimer) containing two Na^+ ions fall within the range of the experimentally measured CCS for D2 and D3, respectively. Although the predicted CCS of $[2GA + 2Na]^{2+}$ ions fall within the range of both D1 and D2, the strong preference for formation of D2 in non-polar solvents suggests that D1 is most likely the parallel double helix and D2 is the antiparallel double helix.

Solution-phase HDX combined with IM-MS provides new information about the hydrogen-bonding network of specific conformers. HDX is consistent with the presence of two ion populations, which are also revealed by distinct IM-MS arrival-time distributions. Although both dimer and monomer populations contain species that undergo fast HDX, IM-MS ATD clearly shows that D2 contains a higher abundance of ions that undergo slow exchange. That is, for the anti-parallel B-helix the bulky, hydrophobic tryptophan residues are positioned at each end of the helix, which limits solvent accessible sites. Conversely, the solvent accessible sites for the parallel dimer extend from the N-terminus of the complex to approximately the middle of each chain, which affords greater accessibility to the hydrogen bonds that stabilize the dimer. This situation is analogous to TRPZIP4 where the bulky tryptophan residues forms a more

compact hydrophobic core that protect the native hydrogen bonds that stabilize the β -hairpin.¹⁶²

CHAPTER VI

SUMMARY

Integrated tempering sampling-molecular dynamics simulations (ITS-MDS) combined with ion mobility spectrometry (IMS) are used to characterize the gas-phase or solution-phase conformational space of several peptide systems. The calculated CCS profiles agree very well with the experimentally measured CCS profiles, which underscore the utility of the method for determining candidate structures as well as the relative abundances of the candidate structures. Ion mobility allows directly visualize the different species with different drift time and consequently to determine their relative proportion at any given time. We have demonstrated that the solution-phase monomer-dimer as well as dimer conformer transition kinetics can be determined by utilizing the ATD profiles of GA monomer and dimer obtained by ESI-IM-MS. The benefit of combining ion mobility measurements with solution-phase H/D exchange is allowing identifications and detail analysis of the solution-phase subgroup conformations, which cannot be uncovered by one method alone.

REFERENCES

- (1) Blackledge, M. *Biophys. J.* **2010**, 98, 2043-2044.
- (2) Wetlaufer, D. B.; C.B. Anfinsen, J. T. E.; Frederic, M. R. In *Advances in Protein Chemistry*; Academic Press: Waltham, Massachusetts, 1981; Vol. 34, p 61-92.
- (3) Peng, Z.-Y.; Wu, L. C.; Matthews, C. R. In *Advances in Protein Chemistry*; Academic Press: Waltham, Massachusetts, 2000; Vol. 53, p 1-30, IN1, 31-47.
- (4) Baumketner, A.; Bernstein, S. L.; Wyttenbach, T.; Lazo, N. D.; Teplow, D. B.; Bowers, M. T.; Shea, J. E. *Protein Sci.* **2006**, 15, 1239-1247.
- (5) Dunker, A. K.; Cortese, M. S.; Romero, P.; Iakoucheva, L. M.; Uversky, V. N. *Febs J.* **2005**, 272, 5129-5148.
- (6) Radivojac, P.; Iakoucheva, L. M.; Oldfield, C. J.; Obradovic, Z.; Uversky, V. N.; Dunker, A. K. *Biophys. J.* **2007**, 92, 1439-1456.
- (7) Radivojac, P.; Obradovic, Z.; Smith, D. K.; Zhu, G.; Vucetic, S.; Brown, C. J.; Lawson, J. D.; Dunker, A. K. *Protein Sci.* **2004**, 13, 71-80.
- (8) Baumketner, A.; Bernstein, S. L.; Wyttenbach, T.; Bitan, G.; Teplow, D. B.; Bowers, M. T.; Shea, J. E. *Protein Sci.* **2006**, 15, 420-428.
- (9) Schmit, J. D.; Ghosh, K.; Dill, K. *Biophys. J.* **2011**, 100, 450-458.
- (10) Ashcroft, A. E. *J. Am. Soc. Mass Spectrom.* **2010**, 21, 1087-1096.
- (11) C. Nick Pace, R. W. A., Kevin L. Shaw, *Protein Sci.* **2000**, 9, 1395-1398.
- (12) Whitten, S. T.; Garcia-Moreno E, B. *Biochemistry* **2000**, 39, 14292-14304.
- (13) Kuhlman, B.; Luisi, D. L.; Young, P.; Raleigh, D. P. *Biochemistry* **1999**, 38, 4896-4903.

- (14) Lipsitz, R. S.; Tjandra, N. *Annu. Rev. Biophys. Biomolec. Struct.* **2004**, *33*, 387-413.
- (15) Fenn, J.; Mann, M.; Meng, C.; Wong, S.; Whitehouse, C. *Science* **1989**, *246*, 64-71.
- (16) Karas, M.; Hillenkamp, F. *Anal. Chem.* **1988**, *60*, 2299-2301.
- (17) Tanaka, K.; Waki, H.; Ido, Y.; Akita, S.; Yoshida, Y.; Yoshida, T.; Matsuo, T. *Rapid Commun. Mass Sp.* **1988**, *2*, 151-153.
- (18) Ruotolo, B. T.; Giles, K.; Campuzano, I.; Sandercock, A. M.; Bateman, R. H.; Robinson, C. V. *Science* **2005**, *310*, 1658-1661.
- (19) Bernstein, S. L.; Dupuis, N. F.; Lazo, N. D.; Wytenbach, T.; Condrón, M. M.; Bitan, G.; Teplow, D. B.; Shea, J. E.; Ruotolo, B. T.; Robinson, C. V.; Bowers, M. T. *Nat. Chem.* **2009**, *1*, 326-331.
- (20) Loo, J. A. *Mass Spectrom. Rev.* **1997**, *16*, 1-23.
- (21) Chen, L.; Shao, Q.; Gao, Y.-Q.; Russell, D. H. *J. Phys. Chem. A* **2011**, *115*, 4427-4435.
- (22) Pierson, N. A.; Chen, L.; Valentine, S. J.; Russell, D. H.; Clemmer, D. E. *J. Am. Chem. Soc.* **2011**, *133*, 13810-13813.
- (23) Chen, L.; Gao, Y. Q.; Russell, D. H. *J. Phys. Chem. A* **2012**, *116*, 689-696.
- (24) Wytenbach, T.; vonHelden, G.; Bowers, M. T. *J. Am. Chem. Soc.* **1996**, *118*, 8355-8364.
- (25) Tao, L.; McLean, J. R.; McLean, J. A.; Russell, D. H. *J. Am. Soc. Mass Spectrom.* **2007**, *18*, 1232-1238.

- (26) Ruotolo, B. T.; Verbeck, G. F.; Thomson, L. M.; Gillig, K. J.; Russell, D. H. *J. Am. Chem. Soc.* **2002**, *124*, 4214-4215.
- (27) Pierson, N. A.; Valentine, S. J.; Clemmer, D. E. *J. Phys. Chem. B* **2010**, *114*, 7777-7783.
- (28) Ruotolo, B. T.; Russell, D. H. *J. Phys. Chem. B* **2004**, *108*, 15321-15331.
- (29) Ruotolo, B. T.; Tate, C. C.; Russell, D. H. *J. Am. Soc. Mass Spectrom.* **2004**, *15*, 870-878.
- (30) Damsbo, M.; Kinnear, B. S.; Hartings, M. R.; Ruhoff, P. T.; Jarrold, M. F.; Ratner, M. A. *Proc. Natl. Acad. Sci. U. S. A.* **2004**, *101*, 7215-7222.
- (31) Fernandez-Lima, F. A.; Wei, H.; Gao, Y. Q.; Russell, D. H. *Journal of Physical Chemistry A* **2009**, *113*, 8221-8234.
- (32) Tao, L.; Dahl, D. B.; Perez, L. M.; Russell, D. H. *J. Am. Soc. Mass Spectrom.* **2009**, *20*, 1593-1602.
- (33) Dill, K. A.; Chan, H. S. *Nature Structural Biology* **1997**, *4*, 10-19.
- (34) Canon, F.; Ballivian, R.; Chirot, F.; Antoine, R.; Sarni-Manchado, P.; Lemoine, J.; Dugourd, P. *J. Am. Chem. Soc.* **2011**, *133*, 7847-7852.
- (35) Grabenauer, M.; Wu, C.; Soto, P.; Shea, J. E.; Bowers, M. T. *J. Am. Chem. Soc.* **2010**, *132*, 532-539.
- (36) Albrieux, F.; Calvo, F.; Chirot, F.; Vorobyev, A.; Tsybin, Y. O.; Lepere, V.; Antoine, R.; Lemoine, J.; Dugourd, P. *J. Phys. Chem. A* **2010**, *114*, 6888-6896.
- (37) Shao, Q.; Yang, L. J.; Gao, Y. Q. *J. Chem. Phys.* **2009**, *130*, 6.
- (38) Gao, Y. Q. *J. Chem. Phys.* **2008**, *128*, 064105.

- (39) Gao, Y. Q. *J. Chem. Phys.* **2008**, *128*, 134111.
- (40) Yang, L. J.; Shao, Q.; Gao, Y. Q. *J. Phys. Chem. B* **2009**, *113*, 803-808.
- (41) Mason, E. A., McDaniel, E. W. *Transport Properties of Ions in Gases*; Wiley: New York, 1988.
- (42) Mason, E. A., McDaniel, E. W. *The Mobility of Diffusion of Ions in Gases*; Wiley-Interscience: New York, 1973.
- (43) Koomen, J. M.; Ruotolo, B. T.; Gillig, K. J.; McLean, J. A.; Russell, D. H.; Kang, M. J.; Dunbar, K. R.; Fuhrer, K.; Gonin, M.; Schultz, J. A. *Anal. Bioanal. Chem.* **2002**, *373*, 612-617.
- (44) Ruotolo, B. T.; Verbeck, G. F.; Thomson, L. M.; Woods, A. S.; Gillig, K. J.; Russell, D. H. *J. Proteome Res.* **2002**, *1*, 303-306.
- (45) Ruotolo, B. T.; Gillig, K. J.; Woods, A. S.; Egan, T. F.; Ugarov, M. V.; Schultz, J. A.; Russell, D. H. *Anal. Chem.* **2004**, *76*, 6727-6733.
- (46) Woods, A. S.; Ugarov, M.; Egan, T.; Koomen, J.; Gillig, K. J.; Fuhrer, K.; Gonin, M.; Schultz, J. A. *Anal. Chem.* **2004**, *76*, 2187-2195.
- (47) Hilton, G. R.; Jackson, A. T.; Thalassinou, K.; Scrivens, J. H. *Anal. Chem.* **2008**, *80*, 9720-9725.
- (48) Fernandez-Lima, F. A.; Becker, C.; McKenna, A. M.; Rodgers, R. P.; Marshall, A. G.; Russell, D. H. *Anal. Chem.* **2009**, *81*, 9941-9947.
- (49) Becker, C.; Fernandez-Lima, F. A.; Gillig, K. J.; Russell, W. K.; Cologna, S. M.; Russell, D. H. *J. Am. Soc. Mass Spectrom.* **2009**, *20*, 907-914.
- (50) Stone, E. G.; Gillig, K. J.; Ruotolo, B. T.; Russell, D. H. *Int. J. Mass Spectrom.* **2001**, *212*, 519-533.

- (51) Stone, E.; Gillig, K. J.; Ruotolo, B.; Fuhrer, K.; Gonin, M.; Schultz, A.; Russell, D. H. *Anal. Chem.* **2001**, *73*, 2233-2238.
- (52) Sun, W. J.; May, J. C.; Russell, D. H. *Int. J. Mass Spectrom.* **2007**, *259*, 79-86.
- (53) McLean, J. A.; Ruotolo, B. T.; Gillig, K. J.; Russell, D. H. *Int. J. Mass Spectrom.* **2005**, *240*, 301-315.
- (54) Ruotolo, B. T.; Benesch, J. L. P.; Sandercock, A. M.; Hyung, S.-J.; Robinson, C. V. *Nat. Protoc.* **2008**, *3*, 1139(14).
- (55) Valentine, S. J.; Counterman, A. E.; Clemmer, D. E. *J. Am. Soc. Mass Spectrom.* **1999**, *10*, 1188-1211.
- (56) Clemmer Collision cross-section Database <http://www.indiana.edu/~clemmer/> accessed on August 2007.
- (57) Vonhelden, G.; Wyttenbach, T.; Bowers, M. T. *Science* **1995**, *267*, 1483-1485.
- (58) Hudgins, R. R.; Woenckhaus, J.; Jarrold, M. F. *Int. J. Mass Spectrom.* **1997**, *165-166*, 497-507.
- (59) Hoaglund-Hyzer, C. S.; Counterman, A. E.; Clemmer, D. E. *Chem. Rev.* **1999**, *99*, 3037-3080.
- (60) Kinnear, B. S.; Hartings, M. R.; Jarrold, M. F. *J. Am. Chem. Soc.* **2001**, *123*, 5660-5667.
- (61) Baker, E. S.; Dupuis, N. F.; Bowers, M. T. *J. Phys. Chem. B* **2009**, *113*, 1722-1727.
- (62) Uetrecht, C.; Barbu, I. M.; Shoemaker, G. K.; van Duijn, E.; HeckAlbert, J. R. *Nat Chem* **2011**, *3*, 126-132.

- (63) Bayly, C. I.; Cieplak, P.; Cornell, W.; Kollman, P. A. *J. Phys. Chem.* **1993**, 97, 10269-10280.
- (64) Cieplak, P.; Cornell, W. D.; Bayly, C.; Kollman, P. A. *J. Comput. Chem.* **1995**, 16, 1357-1377.
- (65) Pigache, A.; Cieplak, P.; Dupradeau, F. Y. *Abstracts of Papers of the American Chemical Society, 227th National Meeting of the American Chemical Society* **2004**.
- (66) Feig, M.; Karanicolas, J.; Brooks Iii, C. L. *J. Mol. Graph. Model.* **2004**, 22, 377-395.
- (67) Feig, M.; Karanicolas, J.; Brooks, C. L.; Elsevier Science Inc: 2004, p 377-395.
- (68) Robert L, B. *Curr. Opin. Struc. Biol.* **1993**, 3, 84-91.
- (69) Schmid, F. X.; Baldwin, R. L. *J. Mol. Biol.* **1979**, 135, 199-215.
- (70) Miranker, A.; Robinson, C.; Radford, S.; Aplin, R.; Dobson, C. *Science* **1993**, 262, 896-900.
- (71) Linderstrom-Lang, K. U. *Symposium on protein structure. Edited by Neuberger A. London: Methuen* **1958**, 23-34.
- (72) Englander, S. W.; Sosnick, T. R.; Englander, J. J.; Mayne, L. *Curr. Opin. Struc. Biol.* **1996**, 6, 18-23.
- (73) Wales, T. E.; Engen, J. R. *Mass Spectrom. Rev.* **2006**, 25, 158-170.
- (74) Bohrer, B. C.; Atlasevich, N.; Clemmer, D. E. *J. Phys. Chem. B* **2011**, 115, 4509-4515.
- (75) Cochran, A. G.; Skelton, N. J.; Starovasnik, M. A. *Proc. Natl. Acad. Sci. U. S. A.* **2001**, 98, 5578-5583.

- (76) Takekiyo, T.; Wu, L.; Yoshimura, Y.; Shimizu, A.; Keiderling, T. A. *Biochemistry* **2009**, *48*, 1543-1552.
- (77) Yang, W. Y.; Pitera, J. W.; Swope, W. C.; Gruebele, M. *J. Mol. Biol.* **2004**, *336*, 241-251.
- (78) Roitberg, A. E.; Okur, A.; Simmerling, C. *J. Phys. Chem. B* **2007**, *111*, 2415-2418.
- (79) Zhang, J.; Qin, M.; Wang, W. *Proteins* **2006**, *62*, 672-685.
- (80) Knochenmuss, R. *Analyst* **2006**, *131*, 966-986.
- (81) Chin, W.; Piuze, F.; Dimicoli, I.; Mons, M. *Phys. Chem. Chem. Phys.* **2006**, *8*, 1033-1048.
- (82) Hu, J.; Barbour, L. J.; Gokel, G. W. *Proc. Natl. Acad. Sci. U. S. A.* **2002**, *99*, 5121-5126.
- (83) Sawyer, H. A.; Marini, J. T.; Stone, E. G.; Ruotolo, B. T.; Gillig, K. J.; Russell, D. H. *J. Am. Soc. Mass Spectrom.* **2005**, *16*, 893-905.
- (84) Hunter, E. P. L.; Lias, S. G. *J. Phys. Chem. Ref. Data* **1998**, *27*, 413-656.
- (85) Wilmot, C. M.; Thornton, J. M. *J. Mol. Biol.* **1988**, *203*, 221-232.
- (86) Rao, C. P.; Nagaraj, R.; Rao, C. N. R.; Balaram, P. *Biochemistry* **1980**, *19*, 425-431.
- (87) Prasad, B. V. V.; Shamala, N.; Nagaraj, R.; Chandrasekaran, R.; Balaram, P. *Biopolymers* **1979**, *18*, 1635-1646.
- (88) Compagnon, I.; Oomens, J.; Meijer, G.; von Helden, G. *J. Am. Chem. Soc.* **2006**, *128*, 3592-3597.

- (89) McLean, J. R.; McLean, J. A.; Wu, Z. X.; Becker, C.; Perez, L. M.; Pace, C. N.; Scholtz, J. M.; Russell, D. H. *J. Phys. Chem. B* **2010**, *114*, 809-816.
- (90) Kohtani, M.; Kinnear, B. S.; Jarrold, M. F. *J. Am. Chem. Soc.* **2000**, *122*, 12377-12378.
- (91) Vaden T. D., G. S. A., de Boer T. S. J. A., Steill. J. D., Oomens J., Snoek L. C. *J. Am. Chem. Soc* **2008**, *130*, 14640-14650.
- (92) Ketchum, R.; Hu, W.; Cross, T. *Science* **1993**, *261*, 1457-1460.
- (93) Urry, D. W.; Mayers, D. F.; Haider, J. *Biochemistry* **1972**, *11*, 487-493.
- (94) Veatch, W. R.; Fossel, E. T.; Blout, E. R. *Biochemistry* **1974**, *13*, 5249-5256.
- (95) Bano, M. C.; Braco, L.; Abad, C. *FEBS Letters* **1989**, *250*, 67-71.
- (96) Chitta, R.; Rempel, D.; Gross, M. *J. Am. Soc. Mass Spectrom.* **2009**, *20*, 1813-1820.
- (97) Mori, T.; Okamoto, Y. *J. Chem. Phys.* **2009**, *131*, 6.
- (98) Roux, B.; Karplus, M. *Annu. Rev. Biophys. Biomolec. Struct.* **1994**, *23*, 731-761.
- (99) Chen, Y.; Wallace, B. A. *Biopolymers* **1997**, *42*, 771-781.
- (100) Wallace, B. A. *Biopolymers* **1983**, *22*, 397-402.
- (101) Burkhardt, B. M.; Li, N.; Langs, D. A.; Pangborn, W. A.; Duax, W. L. *Proc. Natl. Acad. Sci.* **1998**, *95*, 12950-12955.
- (102) Burkhardt, B. M.; Gassman, R. M.; Langs, D. A.; Pangborn, W. A.; Duax, W. L. *Biophys. J.* **1998**, *75*, 2135-2146.

- (103) Fernandez-Lima, F. A.; Becker, C.; Gillig, K.; Russell, W. K.; Nascimento, M. A. C.; Russell, D. H. *J. Phys. Chem. A* **2008**, *112*, 11061-11066.
- (104) Witkop, B. *J. Am. Chem. Soc.* **1964**, *86*, 1848-1853.
- (105) Hwang, S.; Shao, Q.; Williams, H.; Hilty, C.; Gao, Y. Q. *J. Phys. Chem. B* **2011**, *115*, 6653-6660.
- (106) Tucker, W. A.; Sham, S.; Hinton, J. F. *Biochemistry* **2001**, *40*, 11676-11686.
- (107) Ketchum, R. R.; Lee, K. C.; Huo, S.; Cross, T. A. *J. Biomol. NMR* **1996**, *8*, 1-14.
- (108) Hawkes, G. E.; Lu-Yun, L.; Randall, E. W.; Sales, K. D.; Curzon, E. H. In *European Journal of Biochemistry*; Wiley-Blackwell: 1987; Vol. 166, p 437-445.
- (109) Abdul-Manan, N.; Hinton, J. F. *Biochemistry* **1994**, *33*, 6773-6783.
- (110) Zheng, H.; Chruszcz, M.; Lasota, P.; Lebioda, L.; Minor, W. *J. Inorg. Biochem.* **2008**, *102*, 1765-1776.
- (111) Dougherty, D. A. *Science* **1996**, *271*, 163-168.
- (112) Page, M. J.; Di Cera, E. *Physiol. Res.* **2006**, *86*, 1049-1092.
- (113) Kohtani, M.; Jarrold, M. F.; Wee, S.; O'Hair, R. A. J. *J. Phys. Chem. B* **2004**, *108*, 6093-6097.
- (114) Cotton, F. A., Wilkinson, G. *Advanced Inorganic Chemistry, John Wiley & Sons: New York* **1988**, *5th ed.*, p124.
- (115) Kabsch, W.; Sander, C. *Biopolymers* **1983**, *22*, 2577-2637.
- (116) Aqvist, J. *J. Phys. Chem.* **1990**, *94*, 8021-8024.

- (117) Auffinger, P.; Cheatham, T. E.; Vaiana, A. C. *J. Chem. Theory Comput.* **2007**, *3*, 1851-1859.
- (118) Chen, A. A.; Pappu, R. V. *J. Phys. Chem. B* **2007**, *111*, 11884-11887.
- (119) Lee, S.-W.; Freivogel, P.; Schindler, T.; Beauchamp, J. L. *J. Am. Chem. Soc.* **1998**, *120*, 11758-11765.
- (120) Morsa, D.; Gabelica, V.; De Pauw, E. *Anal. Chem.* **2011**, *83*, 5775-5782.
- (121) Polfer, N. C.; Oomens, J.; Dunbar, R. C. *ChemPhysChem* **2008**, *9*, 579-589.
- (122) Polfer, N. C.; Paizs, B.; Snoek, L. C.; Compagnon, I.; Suhai, S.; Meijer, G.; von Helden, G.; Oomens, J. *J. Am. Chem. Soc.* **2005**, *127*, 8571-8579.
- (123) Bush, M. F.; Forbes, M. W.; Jockusch, R. A.; Oomens, J.; Polfer, N. C.; Saykally, R. J.; Williams, E. R. *J. Phys. Chem. A* **2007**, *111*, 7753-7760.
- (124) Prell, J. S.; Demireva, M.; Oomens, J.; Williams, E. R. *J. Am. Chem. Soc.* **2008**, *131*, 1232-1242.
- (125) Kourie, J. I.; Henry, C. L. *Clin. Exp. Pharmacol. P.* **2002**, *29*, 741-753.
- (126) Shai, Y. *Biochim. Biophys. Acta-Biomembr.* **1999**, *1462*, 55-70.
- (127) Dobson, C. M. *Nature* **2003**, *426*, 884-890.
- (128) White, S. H.; Wimley, W. C. *Annu. Rev. Biophys. Biomolec. Struct.* **1999**, *28*, 319-365.
- (129) Ramamoorthy, A.; Lee, D.-K.; Santos, J. S.; Henzler-Wildman, K. A. *J. Am. Chem. Soc.* **2008**, *130*, 11023-11029.

- (130) Fox, C. B.; Wayment, J. R.; Myers, G. A.; Endicott, S. K.; Harris, J. M. *Anal. Chem.* **2009**, *81*, 5130-5138.
- (131) Reshetnyak, Y. K.; Andreev, O. A.; Segala, M.; Markin, V. S.; Engelman, D. M. *Proc. Natl. Acad. Sci.* **2008**, *105*, 15340-15345.
- (132) Murray, M. M.; Bernstein, S. L.; Nyugen, V.; Condrón, M. M.; Teplow, D. B.; Bowers, M. T. *J. Am. Chem. Soc.* **2009**, *131*, 6316-+.
- (133) Bleiholder, C.; Dupuis, N. F.; Wytténbach, T.; Bowers, M. T. *Nat. Chem.* **2011**, *3*, 172-177.
- (134) Dupuis, N. F.; Wu, C.; Shea, J. E.; Bowers, M. T. *J. Am. Chem. Soc.* **2009**, *131*, 18283-18292.
- (135) Sham, S. S.; Shobana, S.; Townsley, L. E.; Jordan, J. B.; Fernandez, J. Q.; Andersen, O. S.; Greathouse, D. V.; Hinton, J. F. *Biochemistry* **2003**, *42*, 1401-1409.
- (136) Lu, J.-X.; Yau, W.-M.; Tycko, R. *Biophys. J.* **2011**, *100*, 711-719.
- (137) Demmers, J. A. A.; Haverkamp, J.; Heck, A. J. R.; Koeppe, R. E.; Killian, J. A. *Proc. Natl. Acad. Sci.* **2000**, *97*, 3189-3194.
- (138) Allen, T. W.; Andersen, O. S.; Roux, B. *J. Am. Chem. Soc.* **2003**, *125*, 9868-9877.
- (139) van Duijn, E.; Barendregt, A.; Synowsky, S.; Versluis, C.; Heck, A. J. R. *J. Am. Chem. Soc.* **2009**, *131*, 1452-1459.
- (140) Kelkar, D. A.; Chattopadhyay, A. *BBA-Biomembranes* **2007**, *1768*, 2011-2025.
- (141) Arseniev, A. S.; Barsukov, I. L.; Bystrov, V. F.; Lomize, A. L.; Ovchinnikov, Y. A. *FEBS Letters* **1985**, *186*, 168-174.

- (142) Veatch, W. R.; Blout, E. R. *Biochemistry* **1974**, *13*, 5257-5264.
- (143) Doyle, D. A.; Wallace, B. A. *Biophy. J.* **1998**, *75*, 635-640.
- (144) O'Boyle, F.; Wallace, B. A. *Protein Peptide lett.* **2003**, *10*, 9-17.
- (145) Wallace, B. A.; Veatch, W. R.; Blout, E. R. *Biochemistry* **1981**, *20*, 5754-5760.
- (146) Pascal, S. M.; Cross, T. A. *J. Mol. Biol.* **1992**, *226*, 1101-1109.
- (147) Chen, Y.; Tucker, A.; Wallace, B. A. *J. Mol. Biol.* **1996**, *264*, 757-769.
- (148) Cotten, M.; Fu, R.; Cross, T. A. *Biophy. J.* **1999**, *76*, 1179-1189.
- (149) Braco, L.; Abad, C.; Campos, A.; Figueruelo, J. E. *J. Chromatogr. A* **1986**, *353*, 181-192.
- (150) Braco, L.; Bano, C.; Chillaron, F.; Abad, C. *Int. J. Biol. Macromol.* **1988**, *10*, 343-348.
- (151) Zhang, J.; Thurbide, K. B. *J. Chromatogr. A* **2006**, *1101*, 286-292.
- (152) Langs, D. *Science* **1988**, *241*, 188-191.
- (153) Wallace, B.; Ravikumar, K. *Science* **1988**, *241*, 182-187.
- (154) Bouchard, M.; Benjamin, D. R.; Tito, P.; Robinson, C. V.; Dobson, C. M. *Biophy. J.* **2000**, *78*, 1010-1017.
- (155) Chitta, R. K.; Gross, M. L. *Biophy. J.* **2004**, *86*, 473-479.
- (156) Breuker, K.; McLafferty, F. W. *Proc. Natl. Acad. Sci.* **2008**, *105*, 18145-18152.

- (157) Liu, Y.; Smith, D. L. *Journal of the American Society for Mass Spectrometry* **1994**, *5*, 19-28.
- (158) Engen, J. R.; Smithgall, T. E.; Gmeiner, W. H.; Smith, D. L. *Biochemistry* **1997**, *36*, 14384-14391.
- (159) Demmers, J. A. A.; Rijkers, D. T. S.; Haverkamp, J.; Killian, J. A.; Heck, A. J. R. *J. Am. Chem. Soc.* **2002**, *124*, 11191-11198.
- (160) Wytenbach, T.; Bowers, M. T. *J. Phys. Chem. B* **2011**, *115*, 12266-12275.
- (161) Shaw, B. F.; Arthanari, H.; Narovlyansky, M.; Durazo, A.; Frueh, D. P.; Pollastri, M. P.; Lee, A.; Bilgicer, B.; Gygi, S. P.; Wagner, G.; Whitesides, G. M. *J. Am. Chem. Soc.*, *132*, 17411-17425.
- (162) Wei, H.; Shao, Q.; Gao, Y. Q. *Phys. Chem. Chem. Phys.* **2010**, *12*, 9292-9299.

VITA

Name: Liuxi Chen

Address: 3225 TAMU, Department of Chemistry, Texas A&M University,
College station TX, 77843

Email Address: liuxic@gmail.com

Education: B.A., Chemistry, University of Science and Technology of China,
Hefei, Anhui, China (July 2005)

Ph.D., Chemistry, Analytical Division, Texas A&M University,
College station, Texas (August 2012)

Affiliations: American Society for Mass Spectrometry, ASMS (since 2006)

Biophysical Society (since 2009)